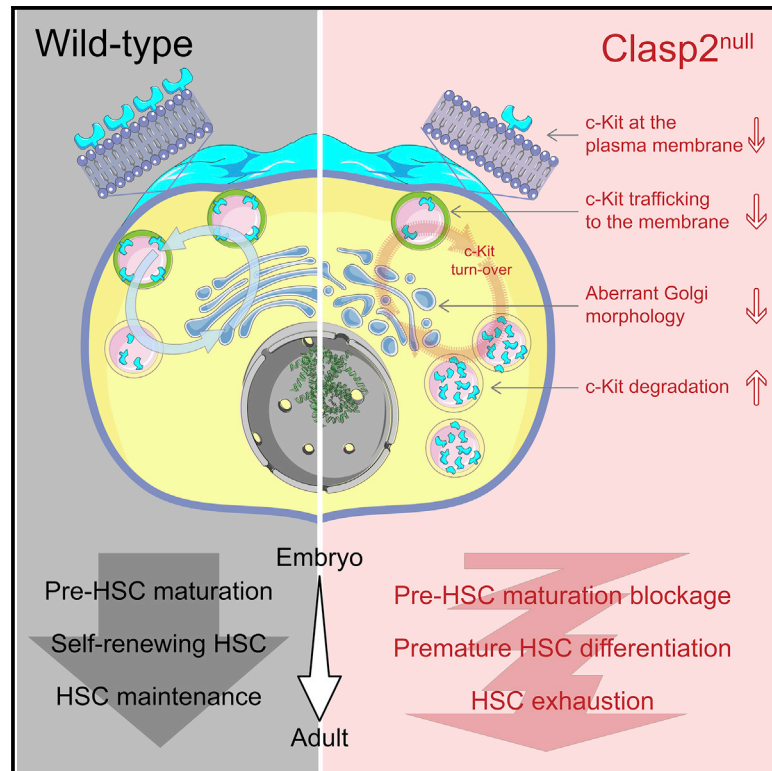


CLASP2 safeguards hematopoietic stem cell properties during mouse and fish development

Graphical abstract



Authors

Anna Klaus, Thomas Clapes, Laurent Yvernogeu, ..., Ihor Smal, Niels Galjart, Catherine Robin

Correspondence

c.robin@hubrecht.eu

In brief

Klaus et al. establish a conserved function for the microtubule-associated protein CLASP2 in HSC generation, maturation, and expansion throughout mouse and zebrafish development. They propose that CLASP2 acts by maintaining Golgi integrity and controlling the correct level of the essential HSC receptor c-Kit on the plasma membrane.

Highlights

- CLASP2 regulates HSC production throughout mouse and zebrafish development
- CLASP2 prevents premature HSC differentiation and loss of self-renewal properties
- CLASP2 controls Golgi apparatus integrity and c-Kit degradation and trafficking in HSCs



Article

CLASP2 safeguards hematopoietic stem cell properties during mouse and fish development

Anna Klaus,¹ Thomas Clapes,¹ Laurent Yvernogeu,^{1,5} Sreya Basu,^{2,5} Bart Weijts,^{1,5} Joris Maas,¹ Ihor Smal,³ Niels Galjart,² and Catherine Robin^{1,4,6,7,*}

¹Hubrecht Institute-KNAW & University Medical Center Utrecht, Uppsalalaan 8, 3584 CT Utrecht, the Netherlands

²Department of Cell Biology, Erasmus University Medical Center, P.O. Box 2040, 3000 CA Rotterdam, the Netherlands

³Theme Biomedical Sciences and Departments of Cell Biology and Molecular Genetics, Erasmus Medical Center, P.O. Box 2040, 3000 CA Rotterdam, the Netherlands

⁴Regenerative Medicine Center, University Medical Center Utrecht, 3584 EA Utrecht, the Netherlands

⁵These authors contributed equally

⁶Senior author

⁷Lead contact

*Correspondence: c.robin@hubrecht.eu

<https://doi.org/10.1016/j.celrep.2022.110957>

SUMMARY

Hematopoietic stem cells (HSCs) express a large variety of cell surface receptors that are associated with acquisition of self-renewal and multipotent properties. Correct expression of these receptors depends on a delicate balance between cell surface trafficking, recycling, and degradation and is controlled by the microtubule network and Golgi apparatus, whose roles have hardly been explored during embryonic/fetal hematopoiesis. Here we show that, in the absence of CLASP2, a microtubule-associated protein, the overall production of HSCs is reduced, and the produced HSCs fail to self-renew and maintain their stemness throughout mouse and zebrafish development. This phenotype can be attributed to decreased cell surface expression of the hematopoietic receptor c-Kit, which originates from increased lysosomal degradation in combination with a reduction in trafficking to the plasma membrane. A dysfunctional Golgi apparatus in CLASP2-deficient HSCs seems to be the underlying cause of the c-Kit expression and signaling imbalance.

INTRODUCTION

Endowed with multilineage differentiation and long-term self-renewal properties, hematopoietic stem cells (HSCs) have the capacity to replenish the entire blood system throughout life without exhaustion. In all vertebrates, the first HSCs originate during embryonic life (Dzierzak and Bigas, 2018; Klaus and Robin, 2017). Starting at embryonic day 9.5 (E9.5) of mouse development, hemogenic endothelial cells first bud from the endothelium lining the main arteries, undergo endothelial-to-hematopoietic transition (EHT) (Boisset et al., 2010; Jaffredo et al., 1998), and subsequently form intra-aortic hematopoietic clusters (IAHCs) (Boisset et al., 2015; Yokomizo and Dzierzak, 2010), whose numbers peak at E10.5, when the first HSCs can be detected in the aorta of the aorta-gonad-mesonephros (AGM) region (Medvinsky and Dzierzak, 1996; Muller et al., 1994; Yokomizo and Dzierzak, 2010). At E11, IAHCs contain few HSCs and committed erythroid-myeloid progenitors (Boisset et al., 2015; Kumaravelu et al., 2002; Robin et al., 2006); instead they are mainly composed of HSC precursors (pre-HSCs, type I and type II) that progressively mature toward fully transplantable HSCs (Baron et al., 2018; Boisset et al., 2015; Rybtsov et al., 2011; Taoudi et al., 2008; Vink et al., 2020; Zhou et al., 2016; Zhu et al., 2020). IAHC cell maturation starts

in the aorta and is completed after pre-HSCs migrate to the fetal liver (FL) (Kumaravelu et al., 2002; Rybtsov et al., 2016). This wave of maturation, followed by expansion, yields a FL-based HSC pool with adult HSC properties, and these HSCs will colonize the bone marrow (BM), the main site of hematopoiesis in adulthood.

An ever-growing body of evidence emphasizes niche interactions as key for functional HSC production and maintenance. Among signaling molecules acting at the plasma membrane, c-Kit, a tyrosine kinase receptor, and stem cell factor (SCF), its ligand, are crucial for blood development and maintenance of adult HSCs, safeguarding their survival and quiescence (Lee et al., 2020; Li and Johnson, 1994; Sharma et al., 2007; Shin et al., 2014; Thoren et al., 2008). SCF is highly expressed by arterial endothelial and perivascular cells, which provide a vascular niche supporting the self-renewal of adult c-Kit-expressing HSCs (Ding et al., 2012; Xu et al., 2018). Hematopoiesis in embryonic niches such as the yolk sac (YS), AGM, and placenta is also regulated through the c-Kit-SCF signaling axis (Azzoni et al., 2018; Sasaki et al., 2010). For instance, SCF is an important factor for maturation of AGM pre-HSCs *in vitro* (Rybtsov et al., 2014).

The journey of an HSC through the successive anatomical niches involves various processes that rely on the ability of



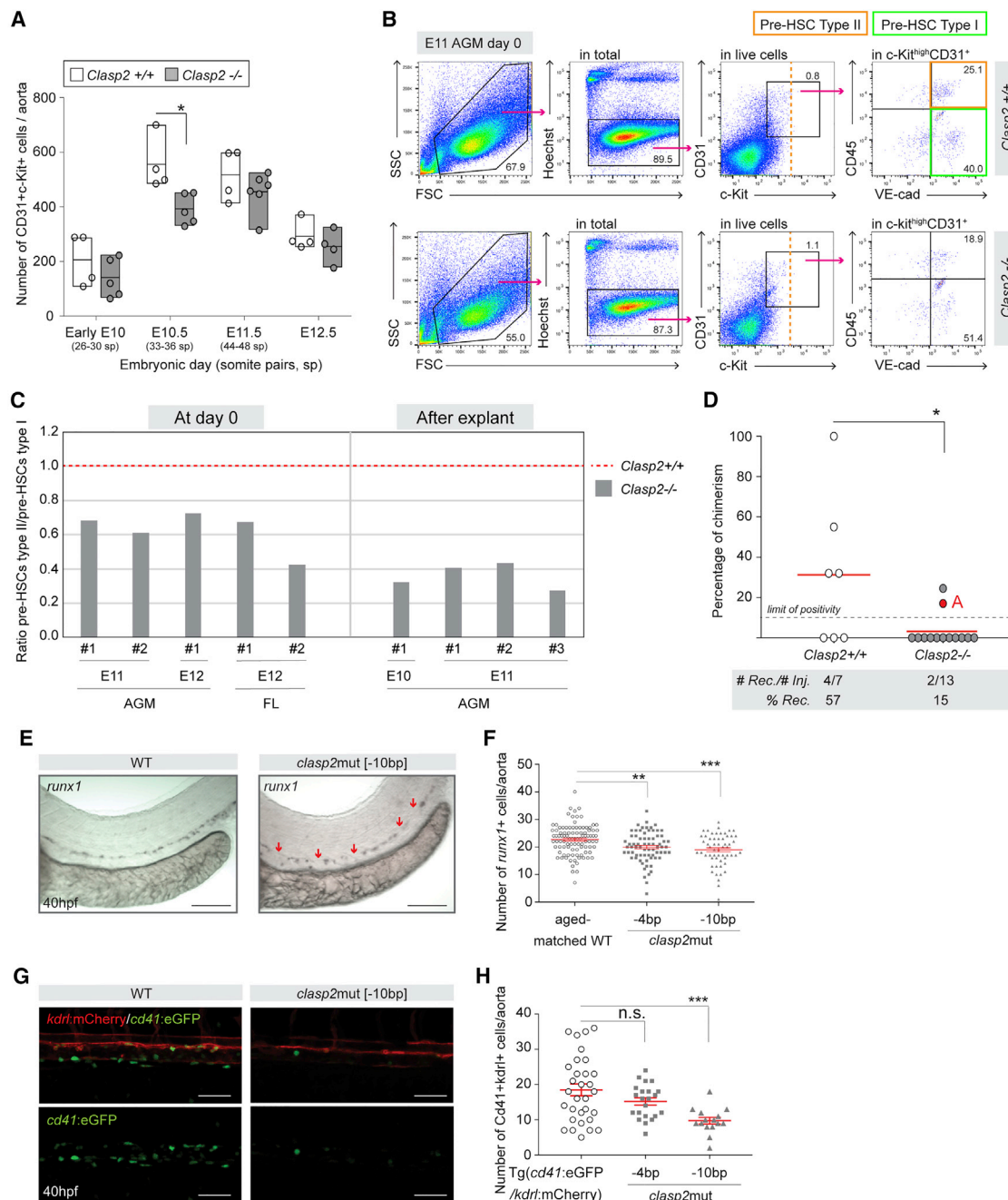


Figure 1. CLASP2 regulates HSPC production in the aortae of mouse and zebrafish embryos

(A) Number of CD31⁺c-Kit⁺ IAH cells per early E10, E10.5, E11.5, and E12.5 *Clasp2*^{+/+} and *Clasp2*^{-/-} aortae (16 *Clasp2*^{+/+}, 20 *Clasp2*^{-/-} embryos, n = 4). One dot represents one embryo.

(B) Representative flow cytometry analyses of type I (green gate, c-Kit⁺CD31⁺VE-cad⁺CD45⁻) and type II (orange gate, c-Kit⁺CD31⁺VE-cad⁺CD45⁺) pre-HSC populations at day 0 in E11 AGMs isolated from *Clasp2*^{+/+} (top panels) and *Clasp2*^{-/-} (bottom panels) embryos (14 *Clasp2*^{+/+}, 8 *Clasp2*^{-/-}, n = 3).

(C) Ratio between the percentages of type II and type I pre-HSCs at day 0 in E11 (n = 2) and E12 (n = 1) AGMs and E12 FLs (n = 2) (left panel) and after explant culture of E10 (n = 1) and E11 (n = 3) AGMs of *Clasp2*^{+/+} and *Clasp2*^{-/-} embryos. #, independent experiments. The ratio for *Clasp2*^{+/+} was set at 1. Average fold decrease: 1.7 ± 0.4 at day 0 (E11/E12) and 2.9 ± 0.6 after explant (E10/E11).

(D) Hematopoietic repopulation (percentage of chimerism) after injection of E11 *Clasp2*^{+/+} and *Clasp2*^{-/-} AGM cells (n = 6, 1 ee/mouse). Dot, one mouse transplant; dashed line, limit of positivity (>10% of chimerism in blood); red line, chimerism average.

(E) Representative images of WISH for *runx1* expression in WT and *clasp2*mut[-10bp] zebrafish embryos (40 hpf). Red arrows, areas with no *runx1*⁺ cells.

(F) Number of *runx1*⁺ cells in the aortae of WT, *clasp2*mut[-4bp], and *clasp2*mut[-10bp] embryos (40 hpf) (n = 5; 97 WT, 71 *clasp2*mut[-4bp], 57 *clasp2*mut[-10bp]).

(legend continued on next page)

HSCs to dynamically modulate intracellular organelles and protein trafficking. This is partly regulated by the microtubule (MT) network, whose behavior and organization are controlled by MT-associated proteins (Akhmanova and Steinmetz, 2015; Bodakuntla et al., 2019; Goodson and Jonasson, 2018). Surprisingly, although the role of MTs in adult human and mouse hematopoietic stem and progenitor cells (HSPCs) has been investigated (Biedzinski et al., 2020; Drabek et al., 2012; Fonseca and Corbeil, 2011; Schwan and Grosse, 2020), no studies have explored MT function in embryonic/fetal hematopoiesis, although pathway analyses of multi-dimensional sequencing have highlighted the potential involvement of cytoskeleton regulation, organization, and biogenesis in the mouse embryonic aorta and zebrafish caudal hematopoietic tissue (CHT), the zebrafish equivalent of the FL (Mascarenhas et al., 2009; Xue et al., 2019; Yvernogeu et al., 2020). Mammalian CLIP-associating protein 1 (CLASP1, Cytoplasmic Linker Associated Protein 1) and CLASP2 are two conserved proteins that bind and stabilize MTs in specific areas of the cell, such as the cellular cortex and kinetochores (Akhmanova et al., 2001; Girao et al., 2020; Lansbergen et al., 2006; Logarinho et al., 2012; Maiato et al., 2003). CLASPs are also involved in non-centrosomal MT nucleation at the Golgi apparatus (Miller et al., 2009) and in regulation of Golgi apparatus morphology itself (Matsui et al., 2015). CLASPs are required for various cellular processes, including directed cell motility (Drabek et al., 2006), focal adhesion turnover and directional vesicle transport (Stehbens et al., 2014), and mitosis (Maffini et al., 2009; Pereira et al., 2006). We previously described a function of CLASP2 in maintenance of HSCs in the mouse adult BM *in vivo* (Drabek et al., 2012). However, it remains unknown whether CLASP2 is involved during embryonic or fetal hematopoiesis in the generation, maturation, and/or expansion of the first HSCs. Here we show that CLASP2 is important to maintain a proper amount of c-Kit at the plasma membrane of pre-HSCs and HSCs, which is crucial to safeguard their stem cell properties and fate throughout mouse and zebrafish development.

RESULTS

CLASP2 regulates IAHC dynamics, pre-HSC maturation, and HSC activity in the aorta of mouse embryos

To determine whether CLASP2 plays a role during embryonic HSC development, we counted CD31⁺c-Kit⁺ IAHC cells in *Clasp2*^{-/-} and *Clasp2*^{+/+} (wild type [WT]) littermates at different time points (Figure 1A). Compared with WT littermates, *Clasp2*^{-/-} embryos had fewer IAHC cells at E10.5, the age when numbers normally peak (Yokomizo and Dzierzak, 2010). This decrease was not due to cell death (Figures S1A and S1B) or defects in proliferation (Figure S1C). IAHC cell production peaked 1 day later, at E11.5, in

Clasp2^{-/-} aortae, reaching a similar number as in *Clasp2*^{+/+} littermates (Figure 1A). Accordingly, increased proliferation of *Clasp2*^{-/-} IAHC cells occurred at E11.5 (Figure S1D) with no increase in cell death (Figure S1E). Despite this increase in proliferation, the peak of *Clasp2*^{-/-} IAHC cells at E11.5 remained lower than in *Clasp2*^{+/+} at E10.5 (Figure 1A).

To decipher whether the delay in IAHC production interfered with cell fate and function, we examined the pre-HSC populations (Boisset et al., 2015; Rybtsov et al., 2011, 2014; Taoudi et al., 2008) by flow cytometry in freshly dissected E11 and E12 AGMs (referred to as day 0), when the numbers of IAHC cells were similar in *Clasp2*^{+/+} and *Clasp2*^{-/-} aortae (Figures 1B and S2A [controls] and S2B). We consistently observed higher percentages of phenotypically defined type I pre-HSCs (c-Kit⁺CD31⁺VE-cad⁺CD45⁻) and lower percentages of type II pre-HSCs (c-Kit⁺CD31⁺VE-cad⁺CD45⁺) in E11 and E12 *Clasp2*^{-/-} compared with *Clasp2*^{+/+} AGMs in each experiment performed, as shown by the lower type II versus type I ratios (Figure 1C, left panel). This partial blockage of pre-HSC maturation was also observed in E12 FLs, where maturation mainly takes place (Rybtsov et al., 2016; Figures 1C, left panel, and S2C). The blockage was amplified after *in vitro* explant culture of E10 and E11 AGMs with cytokines, which normally promotes pre-HSC maturation (Figures 1C, right panel, and S2D). By using another validated combination of surface markers that identifies pre-HSCs type I (CD44^{low}c-Kit⁺VE-cad⁺CD45⁻) and type II (CD44^{high}c-Kit⁺VE-cad⁺CD45⁺) (Oatley et al., 2020; Figure S2E), we confirmed the partial blockage in E11 *Clasp2*^{-/-} compared with *Clasp2*^{+/+} AGMs after explant culture, the type II/type I ratio being 1.7 times lower in *Clasp2*^{-/-} compared with *Clasp2*^{+/+} AGMs.

To test whether the pre-HSC maturation block impaired HSC activity, we performed *in vivo* long-term transplantations of E11 *Clasp2*^{+/+} and *Clasp2*^{-/-} AGM cells. Only 15% of recipients were reconstituted with *Clasp2*^{-/-} cells compared with 57% with *Clasp2*^{+/+} cells (Figure 1D; red lines, mean of chimerism). Reconstitution was not multilineage but lymphoid biased (Figure S3A, top and center panels; injected with *Clasp2*^{+/+} or *Clasp2*^{-/-} cells [mouse A is marked with a red dot in Figure 1D], respectively). Failure to reconstitute secondary recipients revealed a defect in the self-renewal capacity of *Clasp2*^{-/-} cells *in vivo* (Figure S3B). Functional HSCs were thus absent in E11 *Clasp2*^{-/-} aortae. We conclude that CLASP2 controls the timing of IAHC production and pre-HSC maturation to initiate formation of functional HSCs in the aorta.

Conserved role of Clasp2 in HSPC emergence

To determine whether the role of Clasp2 in HSC production was conserved among species, we generated two zebrafish mutant

(G) Representative merge and single GFP fluorescence images of *Tg(cd41:eGFP/kdr:mCherry)* (WT) and *clasp2mut*[-10bp] embryos (background *Tg(cd41:eGFP/kdr:mCherry)*) at 40 hpf.

(H) Number of Cd41⁺kdr⁺ HSPCs per aorta in WT, *clasp2mut*[-4bp], and *clasp2mut*[-10bp] embryos at 40 hpf (n = 3; 31 WT, 25 *clasp2mut*[-4bp], 20 *clasp2mut*[-10bp]).

Line, mean (A and D). Error bars, mean ± SEM (F and H). ***p < 0.001, **p < 0.01, *p < 0.05; n.s., not significant; Mann-Whitney U test (A, D, F, and H). Scale bars: 100 μm (E and G). IAHC, intra-aortic hematopoietic cluster; sp, somite pair; WT, wild type; E, embryonic day; AGM, aorta-gonad-mesonephros; hpf, hour post fertilization; WISH, whole *in situ* hybridization; # Rec, number of reconstituted mice; # Inj, number of injected mice; % Rec, percentage of reconstituted recipients. See also Figures S1–S4.

lines using CRISPR-Cas9 genome editing. We targeted an exon common to most of the *clasp2* variants found in fish, causing a frameshift and a premature STOP codon (Figures S4A and S4B; mutant fish lines are referred to as *clasp2*mut[−4bp] and [−10bp]). Both *clasp2*mut lines displayed robust downregulation of *clasp2* isoforms (Figures S4C and S4D). On average, 25% of embryos from a cross of heterozygous *clasp2*mut displayed a curved body 3 days post fertilization (dpf) (Figures S4E and S4F), and genotyping revealed that these represented homozygous *clasp2*mut embryos. The curved body phenotype was recapitulated when we injected a *clasp2* morpholino oligonucleotide (MO) into embryos (Figure S4G). RT-PCRs showed intron retention in the *clasp2* morphants, indicating that *clasp2* mRNA splicing is blocked (Figure S4H). Rescue of the curved body axis phenotype by injection of WT *clasp2* mRNA in *clasp2*mut (Figures S4I and S4J) confirmed that it was due to loss of *clasp2*. Because the curved body axis is specific for loss of Clasp2 and a convenient mutant screening method, we used it to distinguish *clasp2*mut from aged-matched WT embryos for the rest of the study. *clasp2*mut begin to die at 5 dpf. Many acridine orange⁺ cells, likely apoptotic cells, were observed in the *clasp2*mut neural tube, reflecting an essential role of Clasp2 in fish neuronal development (Figure S5A). In contrast, no difference in acridine orange staining was detected in Cd41⁺Kdr1⁺ HSPCs in the aorta of *clasp2*mut compared with WT embryos (Figure S5B).

To determine whether *clasp2* loss of function interfered with HSPC production in the embryonic aorta, *runx1*⁺ cells were counted after whole *in situ* hybridization (WISH) in *clasp2*mut and WT embryos (Figures 1E and 1F). The number of HSPCs [Cd41⁺Kdr1⁺] was also determined after crossing *clasp2*mut lines with a reporter line for HSPCs and vascular endothelium (*Tg(cd41:eGFP/kdr1:mCherry)*) (Figures 1G and 1H). In both experiments, the number of HSPCs was reduced in *clasp2*mut compared with the WT 40 h post fertilization (hpf) (Figures 1F and 1H). Thus, Clasp2 has a role in formation of the first HSPCs in the aorta of mouse and zebrafish embryos.

CLASP2 regulates HSC self-renewal and prevents HSC exhaustion throughout mouse development

To determine whether CLASP2 is involved in hematopoietic regulation after LAHC emergence, we examined FLs at E14. The phenotypically defined LSK Slam HSC population (Lin^{low/-}CD48^{low/-}SCA-1⁺c-Kit⁺CD150⁺) was present in *Clasp2*^{−/−} FLs (Figure 2A) but less numerous (5,637 ± 1,249 versus 4,290 ± 578 cells per *Clasp2*^{+/+} and *Clasp2*^{−/−} FLs, respectively). No increase in pre-apoptotic (Annexin-V⁺7-AAD[−]) or dead (7-AAD⁺) c-Kit⁺ cells was observed in *Clasp2*^{−/−} FLs (Figures S1F–S1H). However, transplantation of 0.001 and 0.005 embryo equivalents (ee) of *Clasp2*^{−/−} FL cells reconstituted only 1 recipient of 8 (mouse B, red dot) with low chimerism (Figures 2B and 2C; red lines, mean of chimerism), respectively. Reconstitution of mouse B was lymphoid biased (Figure S3A, bottom panel), and none of the secondary recipients were reconstituted (Figure S3B), as reported above for AGM cells. In contrast, all recipients injected with *Clasp2*^{+/+} cells were repopulated with 100% of chimerism (Figures 2B and 2C). Thus, *Clasp2*^{−/−} embryos are depleted in multipotent and self-renewing HSCs in the AGM and FL.

We next tested whether *Clasp2*^{−/−} FL HSCs were progressively exhausted through self-renewal defects by performing a long-term culture-initiating cell (LTC-IC) assay. The ability of sorted E14 FL LSK cells to produce hematopoietic progenitors (CFU-Cs, colony-forming unit cells) was tested up to 4 weeks after co-culture with the supportive stromal cell line MS-5 (Figure 2D). Although the numbers of CFU-Cs produced by *Clasp2*^{+/+} and *Clasp2*^{−/−} LSK cells were similar after 1 and 2 weeks of culture, this number started to decrease after 3 weeks, with almost no CFU-Cs produced at 4 weeks in the *Clasp2*^{−/−} culture (Figure 2D). In comparison, *Clasp2*^{+/+} LSK cells continued to produce CFU-Cs, confirming a self-renewal defect and, therefore, progressive loss of *Clasp2*^{−/−} LSK cells in culture.

Flow cytometry analyses revealed that the progressive exhaustion of HSCs observed in E14 FLs continued *in vivo* in the BM of *Clasp2*^{−/−} neonates (post-natal day 8 [P8]) and young adults (4.5 weeks old) (Figures 2E and 2F). The defect was intrinsic to HSCs and not the result of a defective HSC BM niche, as demonstrated by successful *in vivo* transplantation of total BM cells or LSK-sorted cells from WT donors into irradiated *Clasp2*^{−/−} recipients (Figures S3C and S3D). Sorted LSK cells were transplanted to rule out any possible engraftment of WT-derived BM microenvironment cells that could support WT HSCs. WT HSCs provided high-level multilineage reconstitution in primary (Figures S3C and S3D) and secondary recipients (Figures S3E and S3F), proving their capacity to self-renew in the *Clasp2*^{−/−} BM microenvironment. Overall, our *in vitro* and *in vivo* experiments demonstrate an essential intrinsic role of CLASP2 in proper self-renewal and maintenance of functional HSCs throughout mouse development.

Clasp2 maintains the HSPC pool throughout zebrafish development

After emergence, HSPCs migrate to the CHT in zebrafish embryos (Murayama et al., 2006; Xue et al., 2017) before colonizing the thymus (Bertrand et al., 2007; Kissa et al., 2008) and, ultimately, the kidney marrow (the BM equivalent in fish) (Bertrand et al., 2008; Jin et al., 2007; Murayama et al., 2006; Traver et al., 2003). Because *clasp2*mut begin to die at 5 dpf, our analyses were restricted to earlier time points. We observed progressive loss of Cd41⁺ HSPCs in the CHT of *clasp2*mut compared with aged-matched WT (*Tg(cd41:eGFP/kdr1:mCherry)*) at 52 hpf (Figures 3A and 3B) and 3 dpf (Figures 3C and 3D). These data were confirmed by the decrease in *cmyb*⁺ cells after WISH in the CHT of *clasp2*mut compared with WT siblings (Figures 3E and 3F). Partial hematopoietic phenotype rescue was observed after injection of WT *clasp2* mRNA in *clasp2*mut, confirming that the hematopoietic defect is indeed due to loss of *clasp2* (Figure 3G). HSPC deficiency was also recapitulated in *clasp2* morphants, which drastically lose the *cmyb*⁺ population in the CHT at 3 dpf (Figure 3H). By 5 dpf, the number of Cd41⁺ cells per *clasp2*mut thymus was markedly decreased (Figures 3I and 3J), as expected, because early seeding of the thymus is dependent on HSPCs generated in the AGM and CHT (Bertrand et al., 2008; Murayama et al., 2006). These data were confirmed by a reduced presence or complete absence of the thymic area (*rag1*⁺ T cells) in *clasp2*mut compared with WT siblings at 5 dpf (Figure 3K). Similar to mice, progressive loss of HSPCs in *clasp2*mut zebrafish was not the result of apoptosis because very few acridine orange⁺

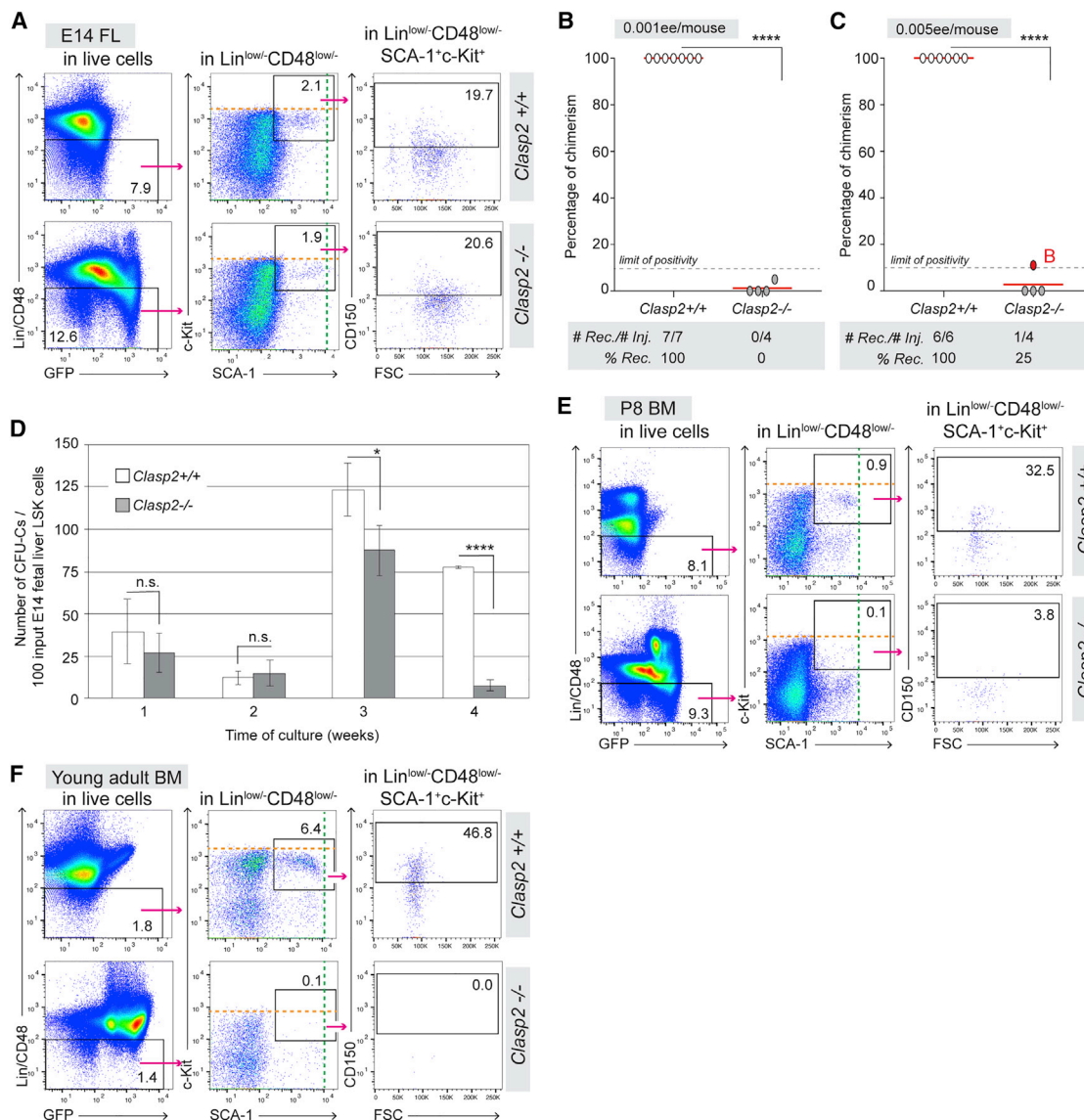


Figure 2. CLASP2 is required to maintain HSC activity throughout mouse development

(A) Gating strategy to analyze phenotypically defined HSCs (Lin^{low}CD48^{low} SCA-1⁺c-Kit⁺CD150⁺CD48^{low}) in E14 FLs (n = 3; 8 Clasp2^{+/+}, 7 Clasp2^{-/-}). (B and C) Hematopoietic repopulation analyses after injection of 0.001 ee (B, n = 3) and 0.005 ee (C, n = 3) of E14 Clasp2^{+/+} and Clasp2^{-/-} FL cells. Red dot, mouse B. (D) Average of CFU-Cs produced weekly per 100 Lin^{low}CD48^{low} SCA-1⁺c-Kit⁺ (LSK) input cells sorted from Clasp2^{+/+} and Clasp2^{-/-} E14 FLs and cultured in the LTC-IC culture system for up to 4 weeks. Shown is 1 representative experiment of 2. Error bars, mean ± SD between triplicates. (E and F) Gating strategy to analyze phenotypically defined HSCs in the BM of Clasp2^{+/+} (top panels) and Clasp2^{-/-} (bottom panels) P8 mice (n = 3) (E) and young adult mice (4.5 weeks old, n = 3) (F). Orange and green dashed lines, highest level of c-Kit and SCA-1 fluorescence, respectively (A, E, and F). Clasp2^{-/-} cells express GFP (as seen in the bottom left plots of A, E, and F; see also STAR Methods). Error bars: mean ± SD (D). ****p < 0.0001, *p < 0.05, Mann-Whitney U test (B and C), Student's t test (D). FL, fetal liver; BM, bone marrow. See also Figures S1 and S3.

apoptotic cells were observed in the aortic region at 40 hpf and in the CHT at 52 hpf and 3 dpf (Figure S5B). Overall, our data demonstrate that Clasp2 also regulates HSPC maintenance throughout zebrafish development.

CLASP2 prevents premature HSPC differentiation

Coinciding with the severe loss of HSPCs in the CHT, we observed a significant increase in neutrophils (Mpx⁺) but not

macrophages (Mpeg⁺) in 3-dpf clasp2mut zebrafish (Figures S6A and S6B), potentially pointing to premature HSPC differentiation. Primitive and definitive hematopoiesis cannot be easily discriminated in clasp2mut because they die after 5 dpf, so we focused on our mouse model to investigate how Clasp2^{-/-} cells might prematurely differentiate. We performed clonogenic assays to examine the production of CFU-Cs in Clasp2^{+/+} and Clasp2^{-/-} E11 AGMs, E14 FLs, and P8 BMs. The numbers and

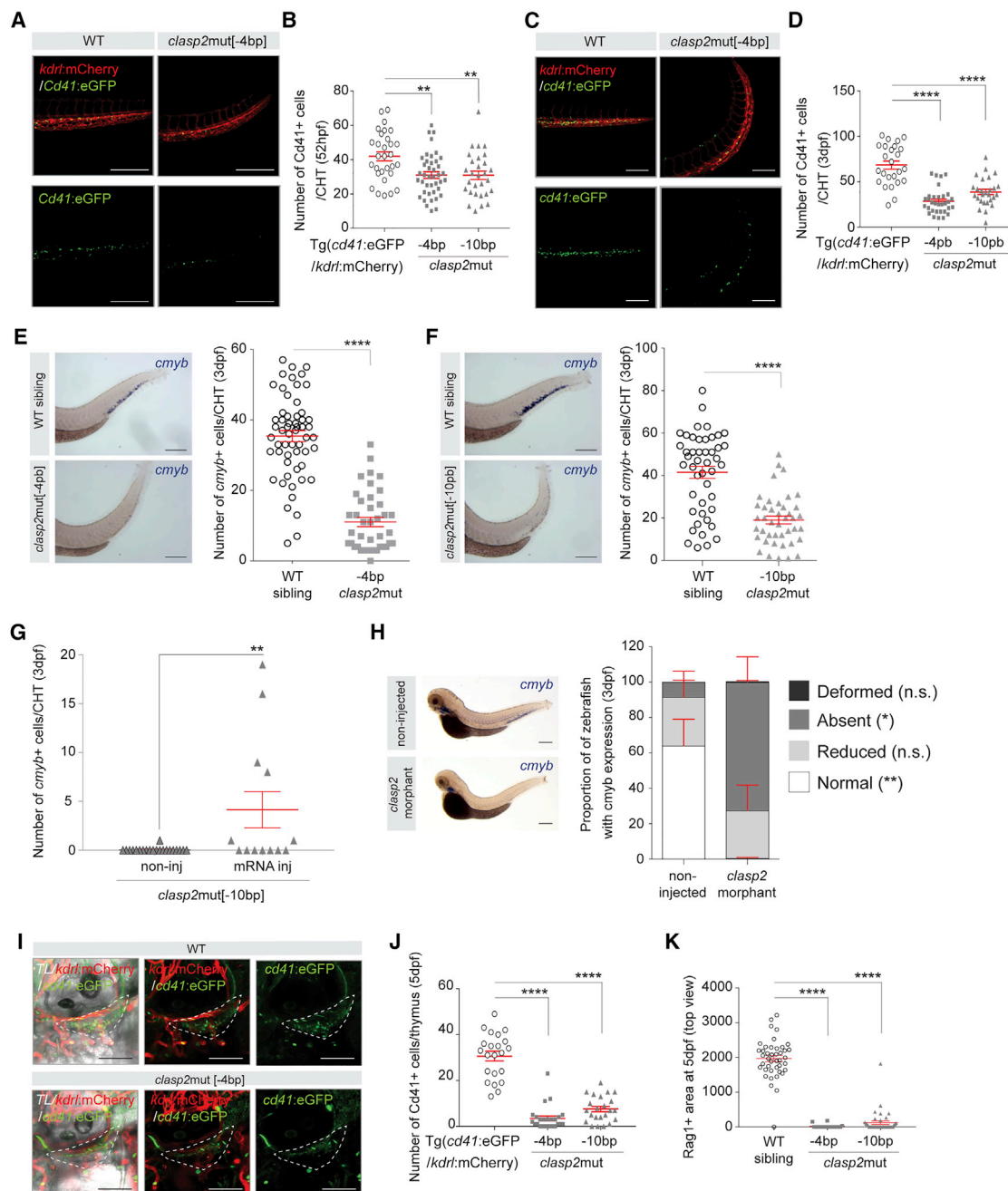


Figure 3. CLASP2 is required to maintain HSPC activity throughout zebrafish development

(A) Representative merge (top panels) and single GFP fluorescence (bottom panels) images of Tg(*cd41:eGFP*/kdr1:mCherry) (WT) and *clasp2mut*[-4bp] zebrafish CHTs (background Tg(*cd41:eGFP*/kdr1:mCherry)) at 52 hpf (n = 3).

(B) Number of Cd41+ cells in the CHT of WT, *clasp2mut*[-4bp] and *clasp2mut*[-10bp] zebrafish embryos at 52 hpf (n = 4–5; 30 WT, 41 *clasp2mut*[-4bp], 29 *clasp2mut*[-10bp] embryos).

(C) Representative merge (top panels) and single GFP fluorescence (bottom panels) images of Tg(*cd41:eGFP*/kdr1:mCherry) and *clasp2mut*[-4bp] zebrafish CHTs at 3 dpf (n = 3).

(D) Number of Cd41+ cells in the CHT of WT, *clasp2mut*[-4bp], and *clasp2mut*[-10bp] zebrafish embryos at 3 dpf (n = 4; 25 WT, 32 *clasp2mut*[-4bp], 27 *clasp2mut*[-10bp]).

(E and F) Representative WISHs and graphs showing the number of *cmyb*+ cells in the CHT of WT sibling, *clasp2mut*[-4bp] (E) and *clasp2mut*[-10bp] (F) embryos at 3 dpf (n = 4, with a total of 57 WT [sibling], 40 *clasp2mut*[-4bp], 46 WT [sibling], and 42 *clasp2mut*[-10bp] embryos). Representative images of WISH for *cmyb* expression are shown on the left.

(G) Number of *cmyb*+ cells per CHT of *clasp2mut*[-10bp] embryos non-injected (non-inj) or injected (inj) with WT *clasp2* mRNA for rescue and analyzed at 3 dpf.

(legend continued on next page)

types of progenitors and cellularity were similar in *Clasp2*^{-/-} and *Clasp2*^{+/-} AGMs at day 0 (Figures 4A and 4B). However, more progenitors were present in *Clasp2*^{-/-} AGMs after explant culture despite lower cellularity (Figures 4C and 4D). These results reflect the *in vivo* situation observed in E14 FLs (Figures 4E and 4F). Importantly, the high number of progenitors in FLs was not due to increased influx of progenitors produced in the YS because this number was similar in *Clasp2*^{-/-} and *Clasp2*^{+/-} YSs (Figure 4G). Because *Clasp2* is highly expressed in the YS, especially in the CD31⁺ endothelial population (Figure 4H), the generation of progenitors in the YS appears to be independent of CLASP2. Thus, the increase in progenitors in FL is most likely due to premature differentiation of pre-HSCs, which are partially blocked toward an HSC fate, as shown above (Figure 1C), and instead directly differentiate into committed progenitors. In support of progressive exhaustion of the HSPC pool, the number of progenitors drastically decreased in the BM of P8 *Clasp2*^{-/-} mice (Figure 4I). This is consistent with the LTC-IC data (Figure 2D) and with the pancytopenia reported previously in *Clasp2*^{-/-} adult mice (Drabek et al., 2012). Thus, CLASP2 maintains the pool of self-renewing HSCs by preventing premature differentiation.

CLASP2 regulates HSPC production by controlling c-kit plasma membrane levels

To determine how CLASP2 might influence the fate of HSCs, we examined important hematopoietic markers, such as SCA-1 and c-Kit, that are known to play a role in differentiation, proliferation, and survival of hematopoietic (stem) cells (Ogawa et al., 1991; Okada et al., 1991; Paral et al., 2018). Flow cytometry analyses of IAHC cells revealed a slight decrease in c-Kit mean fluorescence intensity (MFI) in *Clasp2*^{-/-} embryos at E11 (Figure 5A). By measuring the average fluorescence intensity of c-Kit along the circumference of IAHC cells after whole-mount immunostaining with a c-Kit antibody, using a customized Fiji plugin, we confirmed the reduced levels of c-Kit at the plasma membrane of *Clasp2*^{-/-} IAHC cells (Figures 5B–5D). The decrease, not yet visible at E10, started at E10.5 and persisted at E12 (Figure 5E). Flow cytometry analyses of E14 FL, neonate and adult BM cells, and phenotypically defined HSCs also revealed a progressive decrease in c-Kit MFI in *Clasp2*^{-/-} mice (Figure 5F, left panel; Figures 2A, 2E, and 2F, maximum level of fluorescence intensity indicated with orange dashed lines), which was not the case for SCA-1 and Lin (Figure 5F, center and right panels; Figures 2A, 2E, and 2F, green dashed lines for SCA-1), suggesting a specific sensitivity of c-Kit to the absence of CLASP2. Western blot (WB) experiments performed on Lin⁻ E14 FL cells showed that c-Kit protein levels were strongly decreased in

Clasp2^{-/-} compared with *Clasp2*^{+/-} embryos (Figure 5G), but we did not detect a difference in c-Kit at the transcriptional level (Figure 5H). These results suggest CLASP2 dependent post-translational regulation of c-Kit.

CLASP2 regulates Golgi apparatus morphology and lysosome number in IAHCs and FL HSPCs

Because CLASP2 plays a role in Golgi apparatus organization *in vitro* (Matsui et al., 2015), and the *trans*-Golgi network is a key relay station for vesicular trafficking to the cell surface (Guo et al., 2014; Ravichandran et al., 2020), we examined whether the decreased c-Kit expression at the cell surface might be linked to a potential Golgi defect in *Clasp2*^{-/-} IAHCs. We co-stained for c-Kit and the Golgi apparatus marker GM130 and found an increased Golgi apparatus scattering in *Clasp2*^{-/-} IAHC cells compared with *Clasp2*^{+/-} embryos (Figures 6A–6C). This aberrant Golgi apparatus morphology included the *trans*-Golgi network, as shown by Golgi apparatus reassembly stacking protein GRASP55 staining (Figures S7A–S7C). Remarkably, a similar aberrant Golgi apparatus morphology was also observed in HSPCs in the CHT of *clasp2*mut[–10bp] zebrafish embryos (Figures S7D–S7F), suggesting a universal *in vivo* function of CLASP2 in Golgi apparatus organization and integrity in HSPCs.

Removal of proteins from the surface by lysosomal degradation plays an important role in maintaining the proper levels at the plasma membrane. Immunostaining for lysosomal-associated membrane protein 1 (LAMP-1) showed an increase of lysosomal vesicles in E10.5 *Clasp2*^{-/-} IAHC cells (Figures 6D and 6E), suggesting lysosomal defects in addition to Golgi apparatus abnormalities in HSPCs lacking CLASP2. In agreement with this, we did not detect any differences in LAMP-1 at E10, when no difference in levels of c-Kit at the plasma membrane was observed between *Clasp2*^{+/-} and *Clasp2*^{-/-} embryos (Figures 6F and 5E, left panel). Combined, these data are supportive of abnormal trafficking toward the plasma membrane and/or an increase in c-Kit protein degradation as a basis for c-Kit defects in *Clasp2*^{-/-} HSPCs.

To examine the possibility of increased lysosomal degradation of c-Kit, we cultured E14 FL Lin⁻ cells overnight, untreated or treated with SCF (c-Kit ligand) or Bafilomycin A1 (BafA; a pharmacological inhibitor of lysosomal activity) or with SCF and BafA and measured c-Kit MFI by flow cytometry (Figure 6G). Binding of SCF to c-Kit led to internalization of c-Kit in *Clasp2*^{+/-} and *Clasp2*^{-/-} cells, as measured by a decrease in c-Kit MFI, suggesting that c-Kit maintains its functionality in the absence of CLASP2. Inhibition of lysosomal activity through BafA treatment restored the c-Kit levels in *Clasp2*^{-/-} cells to *Clasp2*^{+/-} levels, indicating that c-Kit undergoes abnormal lysosomal

(H) Proportion of zebrafish embryos with normal or reduced presence or absence of *cmyb* expression in the CHT or deformity at 3 dpf after no injection or injection of *clasp2* morpholinos. Representative cases of WISH for *cmyb* expression are shown on the left. n = 5 with a total of 155 non-inj and 239 inj embryos.

(I) Representative merge (left panels), double (center panels), and single GFP (right panels) fluorescence images of *Tg(cd41:eGFP/kdrl:mCherry)* (WT) and *clasp2*mut[–4bp] (background *Tg(cd41:eGFP/kdrl:mCherry)*) zebrafish thymi (dashed area) at 5 dpf.

(J) Number of *Cd41*⁺ cells in the thymus (dashed areas shown in I) of WT, *clasp2*mut[–4bp] and *clasp2*mut[–10bp] embryos at 5 dpf (n = 3; 22 WT, 25 *clasp2*mut[–4bp], 23 *clasp2*mut[–10bp]).

(K) *Rag1*⁺ area (arbitrary unit) from the top view of the thymus (sum of both thymi) at 5 dpf in WT sibling, *clasp2*mut[–4bp], and *clasp2*mut[–10bp] embryos (n = 2; 42 WT, 20 *clasp2*mut[–4bp], 39 *clasp2*mut[–10bp]).

Green, GFP; ted, *mCherry* (A, C, and I). Mean ± SEM (B, D–H, J, and K). ****p < 0.0001, **p < 0.01, *p < 0.05, Mann-Whitney U test (B, D–H, J, and K). Scale bars, 200 μm (A and C) and 100 μm (I). CHT, caudal hematopoietic tissue. dpf, day post fertilization. See also Figures S4 and S5.

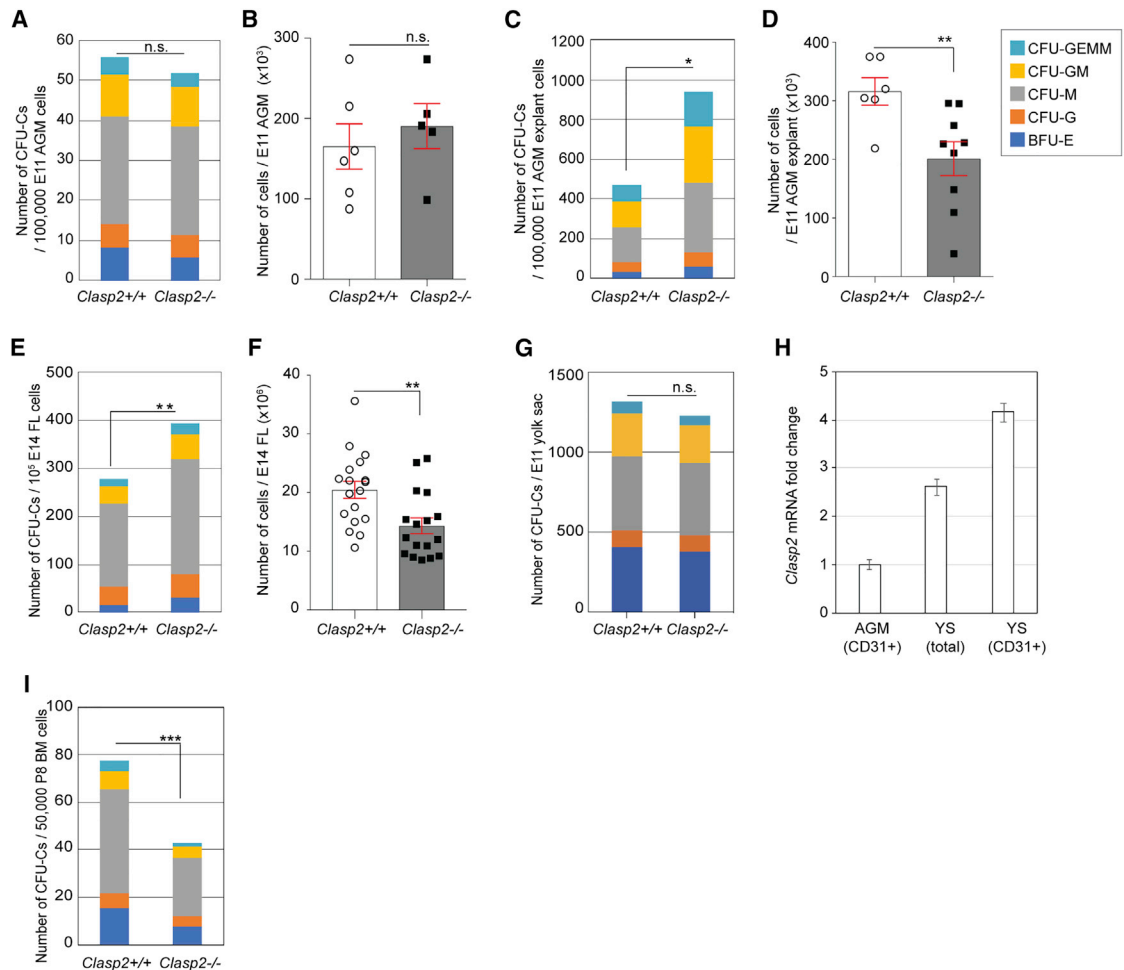


Figure 4. Premature hematopoietic differentiation in *Clasp2*^{-/-} embryos compared with *Clasp2*^{+/+} embryos

(A) Number of CFU-Cs per 100,000 AGM cells of E11 *Clasp2*^{+/+} and *Clasp2*^{-/-} embryos.
 (B) Number of total cells per E11 AGM of *Clasp2*^{+/+} and *Clasp2*^{-/-} embryos at day 0.
 (C) Number of CFU-Cs per 100,000 E11 AGM cells obtained after 3 days of explant culture.
 (D) Number of total cells per E11 AGM after explant culture.
 (E) Number of CFU-Cs per 10⁵ E14 FL cells.
 (F) Number of total cells per E14 FLs.
 (G) Number of CFU-Cs per 1 ee of E11 YS cells.
 (H) Fold change of *clasp2* (alpha) mRNA in total cells and sorted CD31⁺ endothelial cells from E11 WT YSs compared with sorted CD31⁺ endothelial cells from E11 WT AGMs (value set at 1) after qRT-PCR.
 (I) Number of CFU-Cs per 50,000 BM cells obtained from P8 neonates. For E11 AGM at day 0, n = 3 [10 *Clasp2*^{+/+}, 12 *Clasp2*^{-/-}]; E11 AGM explant, n = 5 [12 *Clasp2*^{+/+}, 16 *Clasp2*^{-/-}]; E14 FL, n = 3 [3 *Clasp2*^{+/+}, 4 *Clasp2*^{-/-}]; E11 YS, n = 3 [10 *Clasp2*^{+/+} and 12 *Clasp2*^{-/-}]; P8 BM neonates, n = 2 [2 *Clasp2*^{+/+}, 2 *Clasp2*^{-/-}]. Data are represented as mean ± SEM (B, D, and F) and mean ± SE (H). ***p < 0.001, **p < 0.01, *p < 0.05, Mann-Whitney U test. CFU-GEMM, colony-forming unit-granulocyte-erythroid-macrophage-megakaryocyte; CFU-GM, CFU-granulocyte-macrophage; CFU-M, CFU-macrophage; CFU-G, CFU-granulocyte; BFU-E, burst-forming unit-erythroid; YS, yolk sac. See also Figure S6.

degradation in the absence of CLASP2. Treatment with SCF and BafA increased c-Kit MFI in *Clasp2*^{+/+} cells in comparison with SCF alone but not in *Clasp2*^{-/-} cells. These data suggest that, upon rapid SCF-mediated c-Kit internalization, inhibition of lysosomal degradation is not sufficient to restore c-Kit cell surface levels (as with BafA-only treatment), indicating a limited capacity of *Clasp2*^{-/-} cells to recycle (and/or target newly synthesized) c-Kit to the plasma membrane.

CLASP2 regulates intracellular turnover of c-Kit

Because of the limited number of FL cells, we turned to *Clasp2*^{+/+} and *Clasp2*^{-/-} mouse embryonic stem cells (ESCs), which can be easily expanded and express c-Kit when cultured under conditions that maintain the ground state (Todaro et al., 2019). *Clasp2*^{-/-} ESCs display similar Golgi apparatus defects (Figures S7G and S7H) as *Clasp2*^{-/-} mouse and zebrafish embryos. In addition, c-Kit internalization and lysosomal degradation showed similar

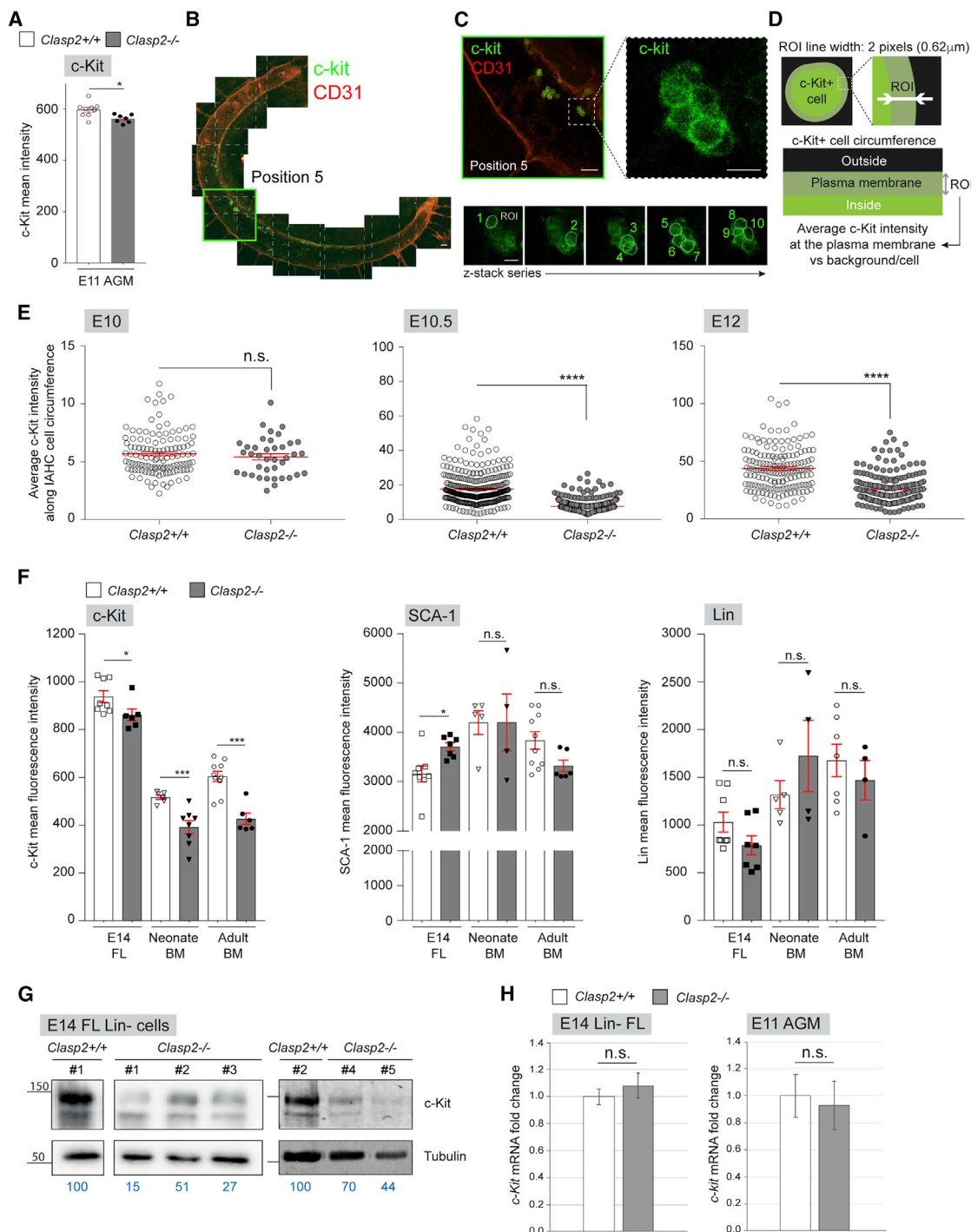


Figure 5. Progressive loss of c-Kit at the plasma membrane of *Clasp2*^{-/-} cells throughout development

(A) MFI of c-Kit measured by flow cytometry in E11 *Clasp2*^{+/+} and *Clasp2*^{-/-} AGMs (9 *Clasp2*^{+/+}, 7 *Clasp2*^{-/-}, n = 7).
 (B) Tile-scale image reconstruction of a whole E10.5 *Clasp2*^{+/+} embryo stained with c-Kit (green) and CD31 (red) antibodies.
 (C) Enlarged image of position 5 shown in (B), with a dashed box outlining the inset, which is shown enlarged on the right and reveals c-Kit fluorescence (green) in an IAHC. Bottom panels: images of this IAHC in various focal planes to draw regions of interest (ROIs) at the maximal fluorescence intensity along the circumference of IAHC cells through a z stack series.
 (D) Illustration of an IAHC cell with the ROI (2 pixels in width) to measure the average c-Kit fluorescence intensity.
 (E) Average MFI of c-Kit along the plasma membrane circumference of IAHC cells in the aortae of E10, E10.5, and E12 *Clasp2*^{+/+} and *Clasp2*^{-/-} embryos after whole-mount immunostaining with c-Kit antibody (E10: 1 *Clasp2*^{+/+}, 2 *Clasp2*^{-/-}; E10.5: 1 *Clasp2*^{+/+}, 1 *Clasp2*^{-/-}; E12: 1 *Clasp2*^{+/+}, 1 *Clasp2*^{-/-}).

(legend continued on next page)

dynamics in *Clasp2*^{-/-} ESCs (Figures 7A and 7B) as in FL cells (Figures 5G and 6G) (i.e., less c-Kit protein under steady-state conditions, reduced c-Kit degradation after BafA treatment, and internalization and degradation of c-Kit after SCF treatment; Figure 7A) and no significant restoration of c-Kit levels in *Clasp2*^{-/-} ESCs when treated with SCF followed by BafA (Figure 7B), indicating rapid degradation of c-Kit prior to inhibition of lysosomal activity. Thus, ESCs appear to be a suitable *in vitro* stem cell model for further analysis of c-Kit.

The imbalance in c-Kit trafficking and degradation in the absence of CLASP2 might originate from altered c-Kit biosynthesis. N-terminal signal sequences are crucial for targeting the nascent protein to the endoplasmic reticulum (ER) (Lennartsson and Ronnstrand, 2012). Concomitant with synthesis and transfer through the ER membrane, asparagine-linked glycosylation occurs in the ER lumen by a membrane-associated enzyme complex, which deposits an oligosaccharide group to the eight asparagine-linked glycosylation sites in its N-terminal domain (Mohanty et al., 2020). Trafficking of c-Kit from the ER to the Golgi apparatus results in enzymatic modification of the sugar chains to the so-called high-mannose-, hybrid-, or complex-type sugars. Because these modifications largely occur in the Golgi apparatus, and this organelle is affected in *Clasp2*^{-/-} ESCs, we first tested whether glycosylation defects might occur in c-Kit in *Clasp2*^{-/-} ESCs. Neither treatment of cell lysates with EndoH1 (an enzyme that cleaves high-mannose-type sugars from glycosylated proteins) nor treatment with PNGase F (Peptide:N-glycosidase F, which cleaves hybrid- and complex-type sugars) revealed an obvious difference in c-Kit glycosylation pattern between *Clasp2*^{+/+} and *Clasp2*^{-/-} ESCs (Figure 7C). EndoH1 hardly cleaved sugars off c-Kit, whereas PNGase F was very efficient, indicating that most of the N-linked sugars on steady state c-Kit in ESCs are of the hybrid or complex type.

Next we tested the effect of tunicamycin, which impairs N-linked ER glycosylation (Elbein, 1984; Heifetz et al., 1979) and prevents trafficking of N-linked glycosylated proteins toward the Golgi complex because of misfolding (Mohanty et al., 2020). Tunicamycin treatment caused the appearance of two lower-molecular-weight bands of c-Kit on WB (marked with N in Figure 7D), which represent newly synthesized, non-glycosylated isoforms (Ribo-Seq analysis [ribosome profiling] of c-Kit translation in ESCs cultured in 2iL confirmed expression of two isoforms; Atlasi et al., 2020). In addition, we detected mature c-Kit (marked with M in Figure 7D), which was synthesized prior to tunicamycin treatment. No difference in the levels of newly synthesized c-Kit was observed between *Clasp2*^{-/-} and *Clasp2*^{+/+} ESCs (Figure 7D; similar N band intensities, indicating similar biosynthesis rates of c-Kit), whereas the ratio of mature versus newly synthesized c-Kit was lower in *Clasp2*^{-/-} ESCs (Figure 7E), indicating that, although synthesis of c-Kit is not

affected, degradation (and, hence, disappearance of mature c-Kit) is increased in *Clasp2*^{-/-} ESCs. Consistent with the decreased expression of c-Kit at the cell surface of *Clasp2*^{-/-} ESCs, we observed a reduction in the phosphorylation of AKT (P-Akt), a well-known downstream target of c-Kit (Figures 7F and 7G; Lennartsson and Ronnstrand, 2012). The mRNA levels of Stat3, another c-Kit target, were also decreased (Figure 7H; Lennartsson and Ronnstrand, 2012; Chaix et al., 2011).

Our data indicate that loss of CLASP2 affects overall Golgi apparatus integrity, including the *trans*-Golgi network, in addition to enhanced lysosomal degradation of c-Kit, and affected trafficking of c-Kit to the plasma membrane, causing reduced downstream signaling, such as AKT and Stat3. Therefore, CLASP2 is important for maintaining a proper amount of c-Kit at the plasma membrane, which is crucial for safeguarding the properties and fate of pre-HSCs and HSCs throughout development.

DISCUSSION

Understanding how HSCs acquire and maintain their stem cell properties *in vivo* is essential for improving HSC production *in vitro*. Here we show that CLASP2, an MT-binding and Golgi-organizing protein, is a key and conserved regulator of HSC formation during embryonic and fetal vertebrate development. Our data demonstrate that CLASP2 is involved in regulation of successive steps, such as EHT dynamics, pre-HSC maturation, and the proper balance between HSC self-renewal and differentiation. Our data suggest that CLASP2 acts in all of these steps by controlling c-Kit levels and, hence, c-kit signaling.

CLASP2 is involved in the first steps of HSC generation in the aorta by regulating EHT dynamics. Defects at this stage might influence subsequent fate decisions and contribute to the partial blockage of pre-HSC maturation and absence of functional HSCs in *Clasp2*^{-/-} AGM, FL, and BM. The requirement for CLASP2 is cell intrinsic and conserved in zebrafish species. The absence of apoptotic markers in the aorta suggests an alternative pre-HSC fate trajectory in *Clasp2*^{-/-} embryos, “skipping” acquisition of a functional HSC identity and prematurely differentiating into more lineage-committed cells. This hypothesis is supported by the lymphoid-biased reconstitution of *Clasp2*^{-/-} AGM and FL cells upon transplantation and the increase in erythroid and myeloid progenitor production after AGM explant and in FLs. Erythro-myeloid progenitors (EMPs) and HSCs emerge from distinct populations of hemogenic endothelial cells in the YS and AGM, respectively (Chen et al., 2011). Our data indicate that CLASP2 is specifically required in HSC- but not EMP-generating hemogenic endothelium. We hypothesize that CLASP2 safeguards the HSC state by preventing exhaustion through defective self-renewal and premature differentiation.

(F) MFI of c-Kit, SCA-1, and Lin markers, measured by flow cytometry in E14 FL and neonate and adult BM cells isolated from *Clasp2*^{+/+} and *Clasp2*^{-/-} embryos and mice (E14 FLs [8 *Clasp2*^{+/+}, 6 *Clasp2*^{-/-} embryos], n = 3; P8 BM [6 *Clasp2*^{+/+}, 8 *Clasp2*^{-/-}], n = 6; adult BM [10 *Clasp2*^{+/+}, 6 *Clasp2*^{-/-}], n = 7).

(G) WBs for c-Kit and tubulin (loading control) on lysates of E14 *Clasp2*^{+/+} and *Clasp2*^{-/-} Lin⁻ FL cells (2 *Clasp2*^{+/+}, 5 *Clasp2*^{-/-}, n = 2). c-Kit intensity is indicated in blue below the gel images; the *Clasp2*^{+/+} culture band was set at 100.

(H) qRT-PCR for c-Kit on Lin⁻ FL cells and total AGM cells from *Clasp2*^{+/+} and *Clasp2*^{-/-} embryos isolated at E14 and E11, respectively.

Error bars: mean ± SEM (A, E, and F), mean ± SD (H). ****p < 0.0001, ***p < 0.001, *p < 0.05, Mann-Whitney U test (A, E, and F), unpaired t test (H). Scale bars, 100 μm (B and C) and 10 μm (C, close up).

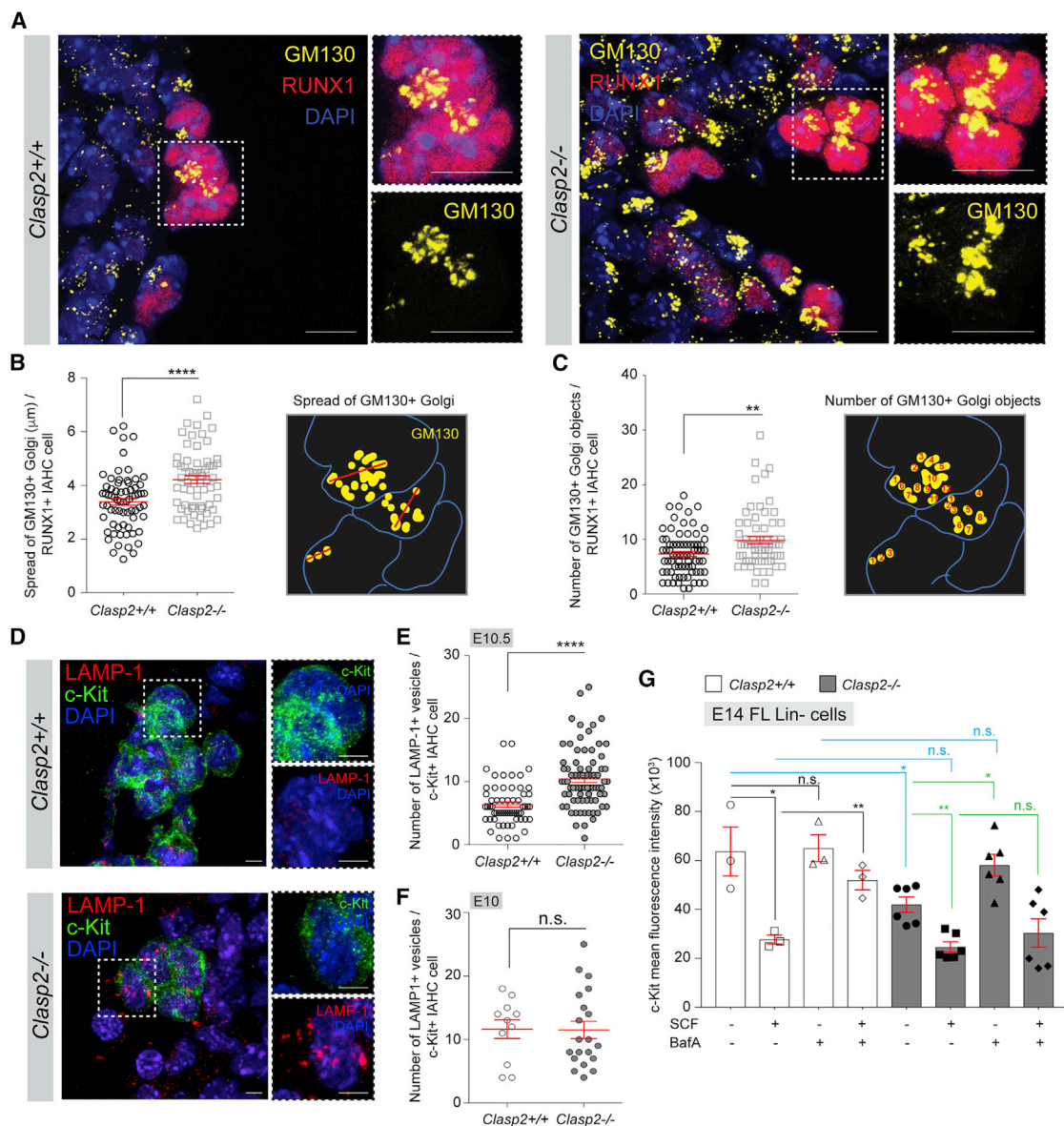


Figure 6. Increased c-Kit degradation and defective trafficking to the plasma membrane in *Clasp2*^{-/-} IAHC cells and Lin⁻ FL cells

(A) Representative images of IAHCs in E10.5 *Clasp2*^{+/+} and *Clasp2*^{-/-} embryos after staining with anti-GM130 (yellow), anti-RUNX1 (red), and DAPI (blue). Dashed boxes are shown enlarged on the right in each main panel, with merges or single (GM130, yellow) fluorescence. (B and C) Spread (B) and number (C) of GM130⁺ Golgi per RUNX1⁺ IAHC cells in E10.5 *Clasp2*^{+/+} and *Clasp2*^{-/-} embryos (n = 3). A schematic on the right side of each graph explains how the spread of Golgi (red lines) or the number of Golgi objects were measured. (D) Representative images of IAHCs in E10.5 *Clasp2*^{+/+} and *Clasp2*^{-/-} embryos after staining with anti-c-Kit (green), anti-LAMP-1 (red), and DAPI (blue). Dashed boxes are shown enlarged on the right of each main panel, with merges of DAPI (blue) and c-Kit (green) or LAMP-1 (red) fluorescence. (E and F) Number of LAMP-1⁺ vesicles per c-Kit⁺ IAHC cells in E10.5 (E) and E10 (F) *Clasp2*^{+/+} and *Clasp2*^{-/-} embryos (n = 2–3). (G) MFI of c-Kit measured by flow cytometry in E14 *Clasp2*^{+/+} and *Clasp2*^{-/-} Lin⁻ FL cells cultured overnight alone or with stem cell factor (SCF; c-Kit ligand), Bafilomycin A1 (BafA), or SCF and BafA (all in triplicates). Data are represented as mean ± SEM (B, C, and E–G). ****p < 0.0001, **p < 0.01, *p < 0.05, Mann-Whitney U test (B, C, E, and F), unpaired t test (G). Scale bars, 10 μm (A) and 5 μm (D). See also Figure S7.

All aortic and FL HSCs reside within the c-Kit^{high} population (Sanchez et al., 1996). We propose that reduced c-Kit expression on the surface of *Clasp2*^{-/-} HSPCs causes at least part of the self-renewal phenotype as well as progressive exhaustion during development. In support of our hypothesis and in concordance

with our data, a decrease in the number of large IAHCs and type II pre-HSCs has been reported in *Kitl* knockouts (*Kitl* encodes SCF), indicating that SCF-c-Kit signaling within the aortic niche regulates this maturation step (Azzoni et al., 2018). *Kitb* knockdown in zebrafish embryos results in specification of fewer

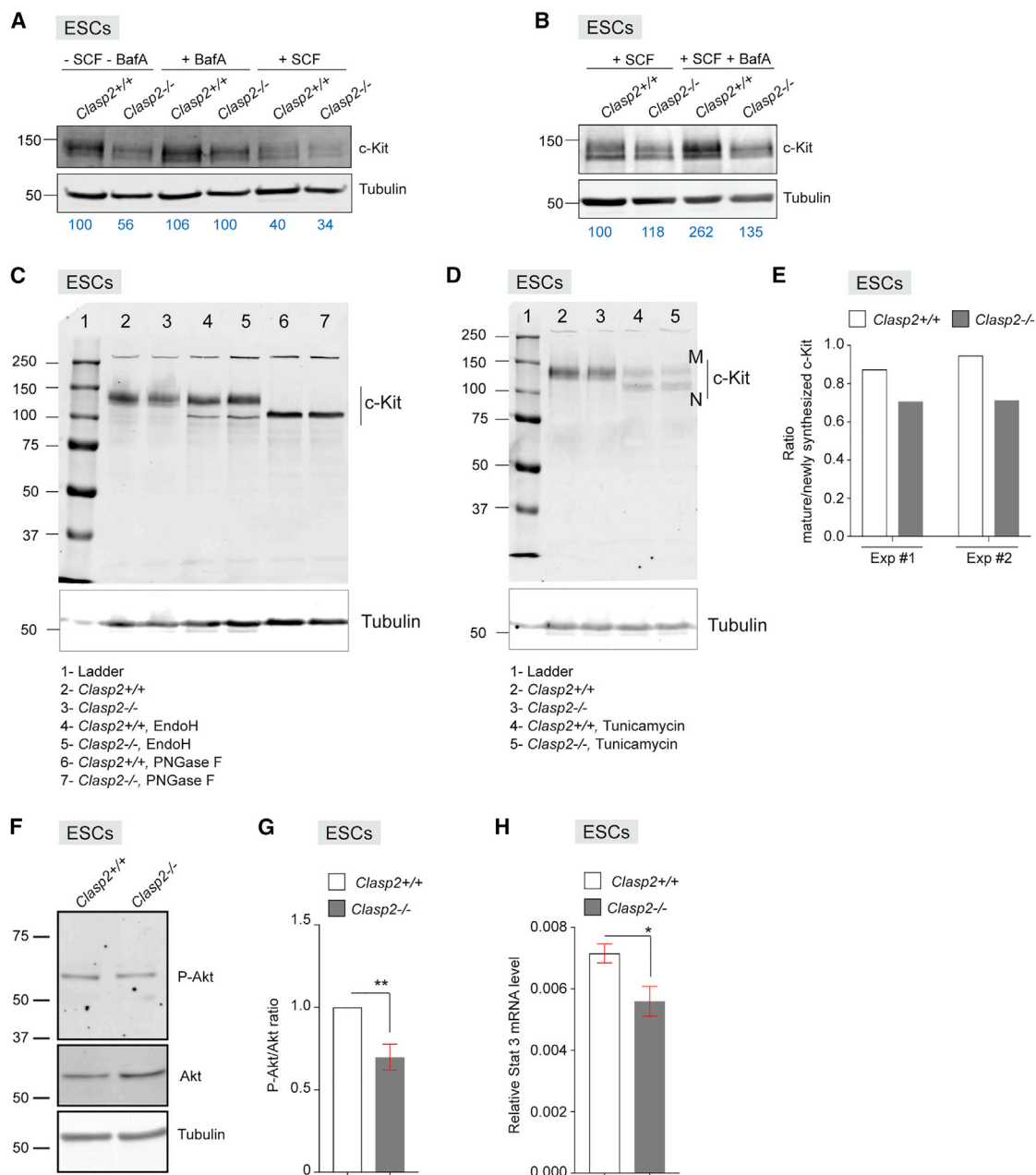


Figure 7. Disturbed c-Kit degradation and trafficking affect downstream targets in *Clasp2*^{-/-} mouse ESCs

(A) WBs for c-Kit and tubulin (loading control) on lysates of *Clasp2*^{+/+} and *Clasp2*^{-/-} mouse embryonic stem cells (mESCs) cultured overnight alone or with BafA or SCF.

(B) WBs for c-Kit and tubulin (loading control) on lysates of *Clasp2*^{+/+} and *Clasp2*^{-/-} mESCs cultured overnight with SCF or SCF followed by BafA.

(A and B) The c-Kit band intensities were quantified using tubulin as a control; these normalized intensities are indicated in blue below gel images, with the left lanes (*Clasp2*^{+/+} culture [A] or *Clasp2*^{+/+} culture with SCF [B]) set at 100 and the other intensities calculated relative to these values.

(C) Mouse *Clasp2*^{+/+} and *Clasp2*^{-/-} ESC lysates were treated with EndoH or PNGase F and examined by WB using antibodies against the indicated proteins (tubulin, loading control). Shown is 1 representative blot of 2.

(D) *Clasp2*^{+/+} and *Clasp2*^{-/-} mESCs were treated overnight with tunicamycin, and lysates were examined by WB using antibodies against the indicated proteins (tubulin, loading control). M, mature c-Kit; N, newly synthesized c-Kit. Shown is 1 representative blot of 2.

(E) Ratio of mature c-Kit levels versus newly synthesized c-Kit, measured by quantifying M and N c-Kit band intensities on WB in *Clasp2*^{+/+} and *Clasp2*^{-/-} mESC lysates in 2 independent experiments (Exp #1 [shown in D] and #2).

(F) WB containing *Clasp2*^{+/+} and *Clasp2*^{-/-} mESC lysate were probed with antibodies against total Akt and phospho-Akt (P-Akt) and against tubulin, which served as a loading control. Shown is 1 representative blot of 4, with two independent sets of biological replicates.

(legend continued on next page)

aortic runx1-expressing HSPCs (Mahony et al., 2018). Thus, the c-Kit surface level in pre-HSCs/HSCs seems to influence the self-renewal/differentiation choice. c-Kit is downregulated upon cell lineage differentiation, where it is mainly co-expressed with myeloid markers (e.g., Mac-1 and Gr1) in the BM (Ogawa et al., 1991). This might explain the lymphoid-biased reconstitution potential of *Clasp2*^{-/-} AGM and FL cells upon transplantation. Modulating the expression of key receptors is an interesting concept to explore whether the generation and maintenance of HSC properties could be improved *in vitro*.

To maintain an optimal level of c-Kit at the cell surface, a balance of c-Kit synthesis, trafficking to the plasma membrane, and degradation is crucial (Lennartsson and Ronnstrand, 2012). Upon ligand binding, most receptor tyrosine kinases, such as c-Kit, are endocytosed and then degraded or recycled back to the cell surface. The choice between lysosomal degradation or recycling is made in early endosomes, and recycling proteins can pass through the *trans*-Golgi network on their way back to the cell surface (Cullen and Steinberg, 2018). Because the Golgi apparatus, including the *trans*-Golgi network, is affected in *Clasp2*^{-/-} cells, trafficking of newly synthesized as well as recycling c-Kit could be affected in the absence of CLASP2. Inhibition of lysosomal activity in E14 FL cells by BafA treatment restored the levels of c-Kit at the plasma membrane of *Clasp2*^{-/-} cells almost to those of *Clasp2*^{+/+} cells treated with BafA. This result is consistent with the notion of enhanced lysosomal degradation of c-Kit in *Clasp2*^{-/-} cells and with somewhat impaired delivery of newly synthesized c-Kit. Upon SCF-mediated internalization of c-Kit, inhibition of lysosomal activity was not sufficient to restore c-Kit levels, suggesting that, in addition to increased degradation, c-Kit plasma membrane recycling is reduced in the absence of CLASP2. We have reported previously that CLASP2 is involved in delivery of acetylcholine receptors to the postsynaptic membrane of the neuro-muscular junction (Basu et al., 2014, 2015; Schmidt et al., 2012) and, more recently, in modulating cardiac sodium channel NaV1.5 activity at the intercalated disk of cardiomyocytes (Marchal et al., 2021). In these studies, as well as in our previous work on the role of CLASP2 in maintenance of adult HSCs (Drabek et al., 2012), we focused on the MT-stabilizing function of CLASP2. Our finding in embryonic (pre-)HSCs lacking CLASP2 is that the trafficking defect of c-Kit is coupled to enhanced c-Kit degradation, which correlates with a higher lysosome number in *Clasp2*^{-/-} cells. Thus, CLASP2 regulates cell surface levels of important proteins in different cell types. Whether all the phenotypes documented here and in other studies are eventually due to an MT-stabilizing and/or growth-promoting role of CLASP2 or whether this fascinating protein has additional activities needs to be examined in future studies.

CLASP2 has been shown to be involved in Golgi apparatus organization in cultured cells (Matsui et al., 2015) and to play a critical role in nucleation of MTs at the *trans*-Golgi (Efimov et al., 2007), aiding vesicular transport of constitutive secretory

pathway components (Miller et al., 2009). Our data reveal, for the first time, a role of CLASP2 in Golgi apparatus organization *in vivo*. This function is conserved in mice and zebrafish because we observed more Golgi scattering in mouse LAHC cells and zebrafish HSPCs in the absence of *Clasp2*. We hypothesize that an aberrant Golgi function affects c-Kit trafficking of newly synthesized as well as recycling protein. Golgi apparatus perturbation seems to affect the lysosomal compartment and cause enhanced degradation of c-Kit in the absence of CLASP2. Our findings bring new insights into the important conserved role of CLASP2 in proper formation of functional HSCs *in vivo*.

Limitations of the study

CLASP2 regulates the level of c-Kit, an important signaling factor at the plasma membrane of HSCs, which significantly affects HSC production and fate. We hypothesize that the low c-Kit expression on the plasma membrane of HSCs in the absence of CLASP2 is caused by aberrant Golgi function affecting c-Kit trafficking and turnover. However, it remains unclear how exactly CLASP2 orchestrates proper c-Kit levels in the various organelles of the secretory route, and further studies are needed to determine whether CLASP2 regulates additional processes in HSCs and other (stem) cell types.

STAR★METHODS

Detailed methods are provided in the online version of this paper and include the following:

- KEY RESOURCES TABLE
- RESOURCE AVAILABILITY
 - Lead contact
 - Materials availability
 - Data and code availability
- EXPERIMENTAL MODEL AND SUBJECT DETAILS
 - Animals
- METHOD DETAILS
 - Generation of *clasp2* mutant lines by CRISPR/Cas9-mediated mutagenesis
 - Zebrafish genotyping
 - Morpholino and mRNA injections
 - Confocal fluorescence imaging of live zebrafish embryos
 - Whole-mount *in situ* hybridization on zebrafish embryos
 - Acridine orange staining
 - Mouse embryo collection, tissue dissection and cell preparation
 - Whole-mount immunostaining on mouse embryos
 - Immunostaining of mouse embryo cryosections
 - Confocal microscopy imaging of mouse whole-mount embryos and cryosections
 - Generation of *Clasp2*^{-/-} embryonic stem cells (ESCs)

(G) Graph representing the relative levels of phospho-Akt to total Akt after normalization to the tubulin loading control.

(H) Graph representing the relative mRNA levels of STAT3 in *Clasp2*^{+/+} and *Clasp2*^{-/-} mESCs. qRT-PCR was performed using STAT3 primers and *Gapdh*, used as a housekeeping control. n = 3 with 3 biological replicates per condition.

**p < 0.01, *p < 0.05, Mann-Whitney U test, mean ± SEM (G and H).

- GM130, GRASP55, LAMP-1 and c-kit immunostaining and quantification
- Flow cytometry analysis and cell sorting
- Magnetic depletion of lineage marker positive cells
- RT-PCR and RT-qPCR
- LTC-IC assay
- *In vitro* clonogenic assay (CFU-C)
- Long-term *in vivo* transplantation assay
- AGM explant culture
- Culture and treatment of Lin[−] fetal liver cells and/or embryonic stem cells (ESCs), c-Kit and glycosylation analyses
- Western blotting
- **QUANTIFICATION AND STATISTICAL ANALYSIS**

SUPPLEMENTAL INFORMATION

Supplemental information can be found online at <https://doi.org/10.1016/j.celrep.2022.110957>.

ACKNOWLEDGMENTS

The authors thank the present and past lab members for helpful discussions and technical help, especially Jean-Charles Boisset, Carla Kroon, Trung Bui, and Rutger Wielink. We also thank the Jeroen den Hertog and Jeroen Bakkers labs for providing reagents, zebrafish lines, and expertise in genome editing and the Catherine Rabouille lab for antibodies. We thank Romualdo Ciau-Uitz (Prof. Roger Patient's Laboratory) for kindly providing ISH probes. We thank Umut Akinci and Alex Maas (Department of Cell Biology, Erasmus MC) for derivation of the *Clasp2*^{−/−} ESCs. We thank the Animal Facility for mouse and zebrafish care and the Optical Imaging Center for confocal microscope access (Hubrecht Institute). We thank Reinier van der Linden (Hubrecht Institute) for help with cell sorting. The authors acknowledge the use of Servier Medical Art image bank to partly create the graphical abstract. This work was supported in the C.R. and N.G. labs by a Landsteiner Stichting voor Bloedtransfusiere-search (LSBR 1025), in the N.G. lab by an NWO-TTW grant (15511), and in the C.R. lab by a European Research Council grant (ERC project number 220-H75001EU/HSCOrigin-309361), a TOP subsidy from NWO/ZonMw (912.15.017), and an UMC Utrecht "Regenerative Medicine & Stem Cells" priority research program.

AUTHOR CONTRIBUTIONS

C.R. and N.G. conceived ideas and designed the research with help from the other authors. C.R., T.C., A.K., and L.Y. performed mouse embryo dissection. C.R. performed mouse transplantation, and T.C. analyzed the mice. T.C. and A.K. performed clonogenic assays. T.C. performed LTC-IC cultures, and A.K. performed explant cultures. T.C. and A.K. performed flow cytometry analyses on mouse embryos. L.Y. performed whole-mount immunostaining and intra-aortic hematopoietic cluster counts. A.K. generated the *clasp2* mutant fish lines and performed all analyses on zebrafish with help from L.Y. for flow cytometry analyses. A.K. performed mouse IF staining with guidance from L.Y. and analyzed the data with C.R., S.B., and N.G. B.W. performed all qRT-PCR on mice and cloned the *clasp2* zebrafish construct for the rescue experiments. S.B. performed western blots and all experiments with ESCs. C.R. performed c-Kit mean intensity measurements. I.S. designed c-Kit intensity measurement and helped with statistical analyses. J.M. performed *runx1* WISH. C.R. analyzed and interpreted the experiments with help from all authors. C.R. created the figures and wrote the paper mostly with help from A.K. and N.G. All authors commented on the manuscript.

DECLARATION OF INTERESTS

The authors declare no competing financial interests.

Received: August 12, 2021

Revised: January 28, 2022

Accepted: May 23, 2022

Published: June 14, 2022

REFERENCES

- Akhmanova, A., Hoogenraad, C.C., Drabek, K., Stepanova, T., Dortland, B., Verkerk, T., Vermeulen, W., Burgering, B.M., De Zeeuw, C.I., Grosveld, F., and Galjart, N. (2001). Clasps are CLIP-115 and -170 associating proteins involved in the regional regulation of microtubule dynamics in motile fibroblasts. *Cell* 104, 923–935. [https://doi.org/10.1016/S0092-8674\(01\)00288-4](https://doi.org/10.1016/S0092-8674(01)00288-4).
- Akhmanova, A., and Steinmetz, M.O. (2015). Control of microtubule organization and dynamics: two ends in the limelight. *Nat. Rev. Mol. Cell Biol.* 16, 711–726. <https://doi.org/10.1038/nrm4084>.
- Atlasi, Y., Jafarnejad, S.M., Gkogkas, C.G., Vermeulen, M., Sonenberg, N., and Stunnenberg, H.G. (2020). The translational landscape of ground state pluripotency. *Nat. Commun.* 11, 1617. <https://doi.org/10.1038/s41467-020-15449-9>.
- Azzoni, E., Frontera, V., McGrath, K.E., Harman, J., Carrelha, J., Nerlov, C., Palis, J., Jacobsen, S.E.W., and de Bruijn, M.F. (2018). Kit ligand has a critical role in mouse yolk sac and aorta-gonad-mesonephros hematopoiesis. *EMBO Rep.* 19. <https://doi.org/10.15252/embr.201745477>.
- Baron, C.S., Kester, L., Klaus, A., Boisset, J.C., Thambyrajah, R., Yvernogeau, L., Kouskoff, V., Lacaud, G., van Oudenaarden, A., and Robin, C. (2018). Single-cell transcriptomics reveal the dynamic of haematopoietic stem cell production in the aorta. *Nat. Commun.* 9, 2517. <https://doi.org/10.1038/s41467-018-04893-3>.
- Basu, S., Sladeczek, S., Martinez de la Pena y Valenzuela, I., Akaaboune, M., Smal, I., Martin, K., Galjart, N., and Brenner, H.R. (2015). CLASP2-dependent microtubule capture at the neuromuscular junction membrane requires LL5β and actin for focal delivery of acetylcholine receptor vesicles. *Mol. Biol. Cell* 26, 938–951. <https://doi.org/10.1091/mbc.E14-06-1158>.
- Basu, S., Sladeczek, S., Pemble, H., Wittmann, T., Slotman, J.A., van Cappellen, W., Brenner, H.R., and Galjart, N. (2014). Acetylcholine receptor (AChR) clustering is regulated both by glycogen synthase kinase 3β (GSK3β)-dependent phosphorylation and the level of CLIP-associated protein 2 (CLASP2) mediating the capture of microtubule plus-ends. *J. Biol. Chem.* 289, 30857–30867. <https://doi.org/10.1074/jbc.M114.589457>.
- Bernut, A., Herrmann, J.L., Kissa, K., Dubremetz, J.F., Gaillard, J.L., Lutfalla, G., and Kremer, L. (2014). Mycobacterium abscessus cording prevents phagocytosis and promotes abscess formation. *Proc. Natl. Acad. Sci. U S A* 111, E943–E952. <https://doi.org/10.1073/pnas.1321390111>.
- Bertrand, J.Y., Kim, A.D., Teng, S., and Traver, D. (2008). CD41+ cmyb+ precursors colonize the zebrafish pronephros by a novel migration route to initiate adult hematopoiesis. *Development* 135, 1853–1862. <https://doi.org/10.1242/dev.015297>.
- Bertrand, J.Y., Kim, A.D., Violette, E.P., Stachura, D.L., Cisson, J.L., and Traver, D. (2007). Definitive hematopoiesis initiates through a committed erythromyeloid progenitor in the zebrafish embryo. *Development* 134, 4147–4156. <https://doi.org/10.1242/dev.012385>.
- Biedzinski, S., Agsu, G., Vianay, B., Delord, M., Blanchoin, L., Larghero, J., Fairv, L., They, M., and Brunet, S. (2020). Microtubules control nuclear shape and gene expression during early stages of hematopoietic differentiation. *EMBO J.* 39, e103957. <https://doi.org/10.15252/emboj.2019103957>.
- Bodakuntla, S., Jijumon, A.S., Villablanca, C., Gonzalez-Billault, C., and Janke, C. (2019). Microtubule-associated proteins: structuring the cytoskeleton. *Trends Cell Biol.* 29, 804–819. <https://doi.org/10.1016/j.tcb.2019.07.004>.
- Boisset, J.C., Andrieu-Soler, C., van Cappellen, W.A., Clapes, T., and Robin, C. (2011). Ex vivo time-lapse confocal imaging of the mouse embryo aorta. *Nat. Protoc.* 6, 1792–1805. <https://doi.org/10.1038/nprot.2011.401>.
- Boisset, J.C., Clapes, T., Klaus, A., Papazian, N., Onderwater, J., Mommaas-Kienhuis, M., Cupedo, T., and Robin, C. (2015). Progressive maturation toward

hematopoietic stem cells in the mouse embryo aorta. *Blood* 125, 465–469. <https://doi.org/10.1182/blood-2014-07-588954>.

Boisset, J.C., van Cappellen, W., Andrieu-Soler, C., Galjart, N., Dzierzak, E., and Robin, C. (2010). In vivo imaging of haematopoietic cells emerging from the mouse aortic endothelium. *Nature* 464, 116–120. <https://doi.org/10.1038/nature08764>.

Chaix, A., Lopez, S., Voisset, E., Gros, L., Dubreuil, P., and De Sepulveda, P. (2011). Mechanisms of STAT protein activation by oncogenic KIT mutants in neoplastic mast cells. *J. Biol. Chem.* 286, 5956–5966. <https://doi.org/10.1074/jbc.M110.182642>.

Chen, M.J., Li, Y., De Obaldia, M.E., Yang, Q., Yzaguirre, A.D., Yamada-Inagawa, T., Vink, C.S., Bhandoola, A., Dzierzak, E., and Speck, N.A. (2011). Erythroid/myeloid progenitors and hematopoietic stem cells originate from distinct populations of endothelial cells. *Cell Stem Cell* 9, 541–552. <https://doi.org/10.1016/j.stem.2011.10.003>.

Cullen, P.J., and Steinberg, F. (2018). To degrade or not to degrade: mechanisms and significance of endocytic recycling. *Nat. Rev. Mol. Cell Biol.* 19, 679–696. <https://doi.org/10.1038/s41580-018-0053-7>.

Ding, L., Saunders, T.L., Enikolopov, G., and Morrison, S.J. (2012). Endothelial and perivascular cells maintain haematopoietic stem cells. *Nature* 487, 457–462. <https://doi.org/10.1038/nature10783>.

Drabek, K., Gutierrez, L., Vermeij, M., Clapes, T., Patel, S.R., Boisset, J.C., van Haren, J., Pereira, A.L., Liu, Z., Akinci, U., et al. (2012). The microtubule plus-end tracking protein CLASP2 is required for hematopoiesis and hematopoietic stem cell maintenance. *Cell Rep.* 2, 781–788. <https://doi.org/10.1016/j.celrep.2012.08.040>.

Drabek, K., van Ham, M., Stepanova, T., Draegestein, K., van Horsen, R., Sayas, C.L., Akhmanova, A., Ten Hagen, T., Smits, R., Fodde, R., et al. (2006). Role of CLASP2 in microtubule stabilization and the regulation of persistent motility. *Curr. Biol.* 16, 2259–2264. <https://doi.org/10.1016/j.cub.2006.09.065>.

Dzierzak, E., and Bigas, A. (2018). Blood development: hematopoietic stem cell dependence and independence. *Cell Stem Cell* 22, 639–651. <https://doi.org/10.1016/j.stem.2018.04.015>.

Efimov, A., Kharitonov, A., Efimova, N., Loncarek, J., Miller, P.M., Andreyeva, N., Gleeson, P., Galjart, N., Maia, A.R., McLeod, I.X., et al. (2007). Asymmetric CLASP-dependent nucleation of noncentrosomal microtubules at the trans-Golgi network. *Dev. Cell* 12, 917–930. <https://doi.org/10.1016/j.devcel.2007.04.002>.

Elbein, A.D. (1984). Inhibitors of the biosynthesis and processing of N-linked oligosaccharide. *CRC Crit. Rev. Biochem.* 16, 21–49. <https://doi.org/10.3109/10409238409102805>.

Fonseca, A.V., and Corbeil, D. (2011). The hematopoietic stem cell polarization and migration: a dynamic link between RhoA signaling pathway, microtubule network and ganglioside-based membrane microdomains. *Commun. Integr. Biol.* 4, 201–204. <https://doi.org/10.4161/cib.4.2.14419>.

Gagnon, J.A., Valen, E., Thyme, S.B., Huang, P., Ahkmetova, L., Pauli, A., Montague, T.G., Zimmerman, S., Richter, C., and Schier, A.F. (2014). Efficient mutagenesis by Cas9 protein-mediated oligonucleotide insertion and large-scale assessment of single-guide RNAs. *PLoS One* 9, e98186. <https://doi.org/10.1371/journal.pone.0098186>.

Girao, H., Okada, N., Rodrigues, T.A., Silva, A.O., Figueiredo, A.C., Garcia, Z., Moutinho-Santos, T., Hayashi, I., Azevedo, J.E., Macedo-Ribeiro, S., and Maiato, H. (2020). CLASP2 binding to curved microtubule tips promotes flux and stabilizes kinetochore attachments. *J. Cell Biol.* 219, jcb.201905080. <https://doi.org/10.1083/jcb.201905080>.

Goodson, H.V., and Jonasson, E.M. (2018). Microtubules and microtubule-associated proteins. *Cold Spring Harbor Perspect. Biol.* 10, a022608. <https://doi.org/10.1101/cshperspect.a022608>.

Guo, Y., Sirkis, D.W., and Schekman, R. (2014). Protein sorting at the trans-Golgi network. *Annu. Rev. Cell Dev. Biol.* 30, 169–206. <https://doi.org/10.1146/annurev-cellbio-100913-013012>.

Heifetz, A., Keenan, R.W., and Elbein, A.D. (1979). Mechanism of action of tunicamycin on the UDP-GlcNAc:dolichyl-phosphate GlcNAc-1-phosphate transferase. *Biochemistry* 18, 2186–2192. <https://doi.org/10.1021/bi00578a008>.

Jaffredo, T., Gautier, R., Eichmann, A., and Dieterlen-Lievre, F. (1998). Intra-aortic hemopoietic cells are derived from endothelial cells during ontogeny. *Development* 125, 4575–4583. <https://doi.org/10.1242/dev.125.22.4575>.

Jin, H., Xu, J., and Wen, Z. (2007). Migratory path of definitive hematopoietic stem/progenitor cells during zebrafish development. *Blood* 109, 5208–5214. <https://doi.org/10.1182/blood-2007-01-069005>.

Kimmel, C.B., Ballard, W.W., Kimmel, S.R., Ullmann, B., and Schilling, T.F. (1995). Stages of embryonic development of the zebrafish. *Dev. Dynam.* 203, 253–310. <https://doi.org/10.1002/aja.1002030302>.

Kissa, K., Murayama, E., Zapata, A., Cortes, A., Perret, E., Machu, C., and Herbolme, P. (2008). Live imaging of emerging hematopoietic stem cells and early thymus colonization. *Blood* 111, 1147–1156. <https://doi.org/10.1182/blood-2007-07-099499>.

Klaus, A., and Robin, C. (2017). Embryonic hematopoiesis under microscopic observation. *Dev. Biol.* 428, 318–327. <https://doi.org/10.1016/j.ydbio.2017.03.008>.

Kumaravelu, P., Hook, L., Morrison, A.M., Ure, J., Zhao, S., Zuyev, S., Ansell, J., and Medvinsky, A. (2002). Quantitative developmental anatomy of definitive haematopoietic stem cells/long-term repopulating units (HSC/RUs): role of the aorta-gonad-mesonephros (AGM) region and the yolk sac in colonisation of the mouse embryonic liver. *Development* 129, 4891–4899.

Laemmli, U.K. (1970). Cleavage of structural proteins during the assembly of the head of bacteriophage T4. *Nature* 227, 680–685. <https://doi.org/10.1038/227680a0>.

Lansbergen, G., Grigoriev, I., Mimori-Kiyosue, Y., Ohtsuka, T., Higa, S., Kitajima, I., Demmers, J., Galjart, N., Houtsmuller, A.B., Grosveld, F., and Akhmanova, A. (2006). CLASPs attach microtubule plus ends to the cell cortex through a complex with LL5β. *Dev. Cell* 11, 21–32. <https://doi.org/10.1016/j.devcel.2006.05.012>.

Lee, D., Kim, D.W., and Cho, J.Y. (2020). Role of growth factors in hematopoietic stem cell niche. *Cell Biol. Toxicol.* 36, 131–144. <https://doi.org/10.1007/s10565-019-09510-7>.

Lennartsson, J., and Ronnstrand, L. (2012). Stem cell factor receptor/c-Kit: from basic science to clinical implications. *Physiol. Rev.* 92, 1619–1649. <https://doi.org/10.1152/physrev.00046.2011>.

Li, C.L., and Johnson, G.R. (1994). Stem cell factor enhances the survival but not the self-renewal of murine hematopoietic long-term repopulating cells. *Blood* 84, 408–414. <https://doi.org/10.1182/blood.v84.2.408.bloodjournal842408>.

Lin, H.F., Traver, D., Zhu, H., Dooley, K., Paw, B.H., Zon, L.I., and Handin, R.I. (2005). Analysis of thrombocyte development in CD41-GFP transgenic zebrafish. *Blood* 106, 3803–3810. <https://doi.org/10.1182/blood-2005-01-0179>.

Logarinho, E., Maffini, S., Barisic, M., Marques, A., Toso, A., Meraldi, P., and Maiato, H. (2012). CLASPs prevent irreversible multipolarity by ensuring spindle-pole resistance to traction forces during chromosome alignment. *Nat. Cell Biol.* 14, 295–303. <https://doi.org/10.1038/ncb2423>.

Maffini, S., Maia, A.R., Manning, A.L., Maliga, Z., Pereira, A.L., Junqueira, M., Shevchenko, A., Hyman, A., Yates, J.R., 3rd, Galjart, N., et al. (2009). Motor-independent targeting of CLASPs to kinetochores by CENP-E promotes microtubule turnover and poleward flux. *Curr. Biol.* 19, 1566–1572. <https://doi.org/10.1016/j.cub.2009.07.059>.

Mahony, C.B., Pasche, C., and Bertrand, J.Y. (2018). Oncostatin M and kit-ligand control hematopoietic stem cell fate during zebrafish embryogenesis. *Stem Cell Rep.* 10, 1920–1934. <https://doi.org/10.1016/j.stemcr.2018.04.016>.

Maiato, H., Fairley, E.A., Rieder, C.L., Swedlow, J.R., Sunkel, C.E., and Earnshaw, W.C. (2003). Human CLASP1 is an outer kinetochore component that regulates spindle microtubule dynamics. *Cell* 113, 891–904. [https://doi.org/10.1016/s0092-8674\(03\)00465-3](https://doi.org/10.1016/s0092-8674(03)00465-3).

Marchal, G.A., Jouni, M., Chiang, D.Y., Pérez-Hernández, M., Podliesna, S., Yu, N., Casini, S., Potet, F., Veerman, C.C., Klerk, M., et al. (2021). Targeting

- the microtubule EB1-CLASP2 complex modulates Nav1.5 at intercalated discs. *Circ. Res.* 129, 349–365. <https://doi.org/10.1161/CIRCRESAHA.120.318643>.
- Mascarenhas, M.I., Parker, A., Dzierzak, E., and Ottersbach, K. (2009). Identification of novel regulators of hematopoietic stem cell development through refinement of stem cell localization and expression profiling. *Blood* 114, 4645–4653. <https://doi.org/10.1182/blood-2009-06-230037>.
- Matsui, T., Watanabe, T., Matsuzawa, K., Kakeno, M., Okumura, N., Sugiyama, I., Itoh, N., and Kaibuchi, K. (2015). PAR3 and aPKC regulate Golgi organization through CLASP2 phosphorylation to generate cell polarity. *Mol. Biol. Cell* 26, 751–761. <https://doi.org/10.1091/mbc.E14-09-1382>.
- Medvinsky, A., and Dzierzak, E. (1996). Definitive hematopoiesis is autonomously initiated by the AGM region. *Cell* 86, 897–906. [https://doi.org/10.1016/s0092-8674\(00\)80165-8](https://doi.org/10.1016/s0092-8674(00)80165-8).
- Miller, P.M., Folkmann, A.W., Maia, A.R.R., Efimova, N., Efimov, A., and Kaverina, I. (2009). Golgi-derived CLASP-dependent microtubules control Golgi organization and polarized trafficking in motile cells. *Nat. Cell Biol.* 11, 1069–1080. <https://doi.org/10.1038/ncb1920>.
- Mohanty, S., P Chaudhary, B., and Zoetewey, D. (2020). Structural insight into the mechanism of N-linked glycosylation by oligosaccharyltransferase. *Biomolecules* 10, 624. <https://doi.org/10.3390/biom10040624>.
- Muller, A.M., Medvinsky, A., Strouboulis, J., Grosveld, F., and Dzierzak, E. (1994). Development of hematopoietic stem cell activity in the mouse embryo. *Immunity* 1, 291–301. [https://doi.org/10.1016/1074-7613\(94\)90081-7](https://doi.org/10.1016/1074-7613(94)90081-7).
- Murayama, E., Kissa, K., Zapata, A., Mordelet, E., Briolat, V., Lin, H.F., Handin, R.I., and Herbomel, P. (2006). Tracing hematopoietic precursor migration to successive hematopoietic organs during zebrafish development. *Immunity* 25, 963–975. <https://doi.org/10.1016/j.immuni.2006.10.015>.
- Oatley, M., Bolukbasi, O.V., Svensson, V., Shvartsman, M., Ganter, K., Zirnigib, K., Pavlovich, P.V., Milchevskaya, V., Foteva, V., Natarajan, K.N., et al. (2020). Single-cell transcriptomics identifies CD44 as a marker and regulator of endothelial to haematopoietic transition. *Nat. Commun.* 11, 586. <https://doi.org/10.1038/s41467-019-14171-5>.
- Ogawa, M., Matsuzaki, Y., Nishikawa, S., Hayashi, S., Kunisada, T., Sudo, T., Kina, T., Nakauchi, H., and Nishikawa, S. (1991). Expression and function of c-kit in hematopoietic progenitor cells. *J. Exp. Med.* 174, 63–71. <https://doi.org/10.1084/jem.174.1.63>.
- Okada, S., Nakauchi, H., Nagayoshi, K., Nishikawa, S., Nishikawa, S., Miura, Y., and Suda, T. (1991). Enrichment and characterization of murine hematopoietic stem cells that express c-kit molecule. *Blood* 78, 1706–1712. <https://doi.org/10.1182/blood.v78.7.1706.1706>.
- Paral, P., Faltusova, K., Molik, M., Renesova, N., Sefc, L., and Necas, E. (2018). Cell cycle and differentiation of Sca-1(+) and Sca-1(-) hematopoietic stem and progenitor cells. *Cell Cycle* 17, 1979–1991. <https://doi.org/10.1080/15384101.2018.1502573>.
- Pereira, A.L., Pereira, A.J., Maia, A.R., Drabek, K., Sayas, C.L., Hergert, P.J., Lince-Faria, M., Matos, I., Duque, C., Stepanova, T., et al. (2006). Mammalian CLASP1 and CLASP2 cooperate to ensure mitotic fidelity by regulating spindle and kinetochore function. *Mol. Biol. Cell* 17, 4526–4542. <https://doi.org/10.1091/mbc.E06-07-0579>.
- Pouthis, F., Girard, P., Lecaudey, V., Ly, T.B.N., Gilmour, D., Boulon, C., Perperkok, R., and Reynaud, E.G. (2008). In migrating cells, the Golgi complex and the position of the centrosome depend on geometrical constraints of the substratum. *J. Cell Sci.* 121, 2406–2414. <https://doi.org/10.1242/jcs.026849>.
- Ravichandran, Y., Goud, B., and Manneville, J.B. (2020). The Golgi apparatus and cell polarity: roles of the cytoskeleton, the Golgi matrix, and Golgi membranes. *Curr. Opin. Cell Biol.* 62, 104–113. <https://doi.org/10.1016/j.ccb.2019.10.003>.
- Renshaw, S.A., Loynes, C.A., Trushell, D.M., Elworthy, S., Ingham, P.W., and Whyte, M.K. (2006). A transgenic zebrafish model of neutrophilic inflammation. *Blood* 108, 3976–3978. <https://doi.org/10.1182/blood-2006-05-024075>.
- Robin, C., and Dzierzak, E. (2005). Hematopoietic stem cell enrichment from the AGM region of the mouse embryo. *Methods Mol. Med.* 105, 257–272. <https://doi.org/10.1385/1-59259-826-9-257>.
- Robin, C., Ottersbach, K., Boisset, J.C., Oziemlak, A., and Dzierzak, E. (2011). CD41 is developmentally regulated and differentially expressed on mouse hematopoietic stem cells. *Blood* 117, 5088–5091. <https://doi.org/10.1182/blood-2011-01-329516>.
- Robin, C., Ottersbach, K., Durand, C., Peeters, M., Vanes, L., Tybulewicz, V., and Dzierzak, E. (2006). An unexpected role for IL-3 in the embryonic development of hematopoietic stem cells. *Dev. Cell* 11, 171–180. <https://doi.org/10.1016/j.devcel.2006.07.002>.
- Rybtsov, S., Batsivari, A., Bilotkach, K., Paruzina, D., Senserrich, J., Nerushev, O., and Medvinsky, A. (2014). Tracing the origin of the HSC hierarchy reveals an SCF-dependent, IL-3-independent CD43(-) embryonic precursor. *Stem Cell Rep.* 3, 489–501. <https://doi.org/10.1016/j.stemcr.2014.07.009>.
- Rybtsov, S., Ivanovs, A., Zhao, S., and Medvinsky, A. (2016). Concealed expansion of immature precursors underpins acute burst of adult HSC activity in foetal liver. *Development* 143, 1284–1289. <https://doi.org/10.1242/dev.131193>.
- Rybtsov, S., Sobiesiak, M., Taoudi, S., Souilhol, C., Senserrich, J., Liakhovitskaia, A., Ivanovs, A., Frampton, J., Zhao, S., and Medvinsky, A. (2011). Hierarchical organization and early hematopoietic specification of the developing HSC lineage in the AGM region. *J. Exp. Med.* 208, 1305–1315. <https://doi.org/10.1084/jem.20102419>.
- Sanchez, M.J., Holmes, A., Miles, C., and Dzierzak, E. (1996). Characterization of the first definitive hematopoietic stem cells in the AGM and liver of the mouse embryo. *Immunity* 5, 513–525. [https://doi.org/10.1016/s1074-7613\(00\)80267-8](https://doi.org/10.1016/s1074-7613(00)80267-8).
- Sasaki, T., Mizuuchi, C., Horio, Y., Nakao, K., Akashi, K., and Sugiyama, D. (2010). Regulation of hematopoietic cell clusters in the placental niche through SCF/Kit signaling in embryonic mouse. *Development* 137, 3941–3952. <https://doi.org/10.1242/dev.051359>.
- Schindelin, J., Arganda-Carreras, I., Frise, E., Kaynig, V., Longair, M., Pietzsch, T., Preibisch, S., Rueden, C., Saalfeld, S., Schmid, B., et al. (2012). Fiji: an open-source platform for biological-image analysis. *Nat. Methods* 9, 676–682. <https://doi.org/10.1038/nmeth.2019>.
- Schmidt, N., Basu, S., Sladeczek, S., Gatti, S., van Haren, J., Treves, S., Piehlage, J., Gajart, N., and Brenner, H.R. (2012). Agrin regulates CLASP2-mediated capture of microtubules at the neuromuscular junction synaptic membrane. *J. Cell Biol.* 198, 421–437. <https://doi.org/10.1083/jcb.201111130>.
- Schwan, C., and Grosse, R. (2020). A tight grip on differentiation: nuclear constriction by microtubules regulates hematopoietic stem cells. *EMBO J.* 39, e107086. <https://doi.org/10.15252/emboj.2020107086>.
- Sharma, Y., Astle, C.M., and Harrison, D.E. (2007). Heterozygous kit mutants with little or no apparent anemia exhibit large defects in overall hematopoietic stem cell function. *Exp. Hematol.* 35, 214.e1–214.e9. <https://doi.org/10.1016/j.exphem.2006.10.001>.
- Shin, J.Y., Hu, W., Naramura, M., and Park, C.Y. (2014). High c-Kit expression identifies hematopoietic stem cells with impaired self-renewal and megakaryocytic bias. *J. Exp. Med.* 211, 217–231. <https://doi.org/10.1084/jem.20131128>.
- Stehbens, S.J., Paszek, M., Pemble, H., Ettinger, A., Gierke, S., and Wittmann, T. (2014). CLASPs link focal-adhesion-associated microtubule capture to localized exocytosis and adhesion site turnover. *Nat. Cell Biol.* 16, 558–570. <https://doi.org/10.1038/ncb2975>.
- Taoudi, S., Gonneau, C., Moore, K., Sheridan, J.M., Blackburn, C.C., Taylor, E., and Medvinsky, A. (2008). Extensive hematopoietic stem cell generation in the AGM region via maturation of VE-cadherin+CD45+ pre-definitive HSCs. *Cell Stem Cell* 3, 99–108. <https://doi.org/10.1016/j.stem.2008.06.004>.
- Thoren, L.A., Liuba, K., Bryder, D., Nygren, J.M., Jensen, C.T., Qian, H., Antonchuk, J., and Jacobsen, S.E.W. (2008). Kit regulates maintenance of quiescent hematopoietic stem cells. *J. Immunol.* 180, 2045–2053. <https://doi.org/10.4049/jimmunol.180.4.2045>.

- Todaro, F., Campolo, F., Barrios, F., Pellegrini, M., Di Cesare, S., Tessarollo, L., Rossi, P., Jannini, E.A., and Dolci, S. (2019). Regulation of kit expression in early mouse embryos and ES cells. *Stem Cell*. 37, 332–344. <https://doi.org/10.1002/stem.2960>.
- Traver, D., Paw, B.H., Poss, K.D., Penberthy, W.T., Lin, S., and Zon, L.I. (2003). Transplantation and in vivo imaging of multilineage engraftment in zebrafish bloodless mutants. *Nat. Immunol.* 4, 1238–1246. <https://doi.org/10.1038/ni1007>.
- Vink, C.S., Calero-Nieto, F.J., Wang, X., Maglito, A., Mariani, S.A., Jawaid, W., Gottgens, B., and Dzierzak, E. (2020). Iterative single-cell analyses define the transcriptome of the first functional hematopoietic stem cells. *Cell Rep.* 31, 107627. <https://doi.org/10.1016/j.celrep.2020.107627>.
- Weijts, B., Tkachenko, E., Traver, D., and Groisman, A. (2017). A four-well dish for high-resolution longitudinal imaging of the tail and posterior trunk of larval zebrafish. *Zebrafish* 14, 489–491. <https://doi.org/10.1089/zeb.2016.1406>.
- Westerfield, M. (2000). *The Zebrafish Book. A Guide for the Laboratory Use of Zebrafish (Danio rerio)*, Fourth Edition (Univ. of Oregon Press).
- Xu, C., Gao, X., Wei, Q., Nakahara, F., Zimmerman, S.E., Mar, J., and Frenette, P.S. (2018). Stem cell factor is selectively secreted by arterial endothelial cells in bone marrow. *Nat. Commun.* 9, 2449. <https://doi.org/10.1038/s41467-018-04726-3>.
- Xue, Y., Liu, D., Cui, G., Ding, Y., Ai, D., Gao, S., Zhang, Y., Suo, S., Wang, X., Lv, P., et al. (2019). A 3D Atlas of hematopoietic stem and progenitor cell expansion by multi-dimensional RNA-seq analysis. *Cell Rep.* 27, 1567–1578.e5. <https://doi.org/10.1016/j.celrep.2019.04.030>.
- Xue, Y., Lv, J., Zhang, C., Wang, L., Ma, D., and Liu, F. (2017). The vascular niche regulates hematopoietic stem and progenitor cell lodgment and expansion via klf6a-ccl25b. *Dev. Cell* 42, 349–362.e4. <https://doi.org/10.1016/j.devcel.2017.07.012>.
- Yokomizo, T., and Dzierzak, E. (2010). Three-dimensional cartography of hematopoietic clusters in the vasculature of whole mouse embryos. *Development* 137, 3651–3661. <https://doi.org/10.1242/dev.051094>.
- Yvernogeau, L., Klaus, A., Maas, J., Morin-Poulard, I., Weijts, B., Schulte-Merker, S., Berezikov, E., Junker, J.P., and Robin, C. (2020). Multispecies RNA tomography reveals regulators of hematopoietic stem cell birth in the embryonic aorta. *Blood* 136, 831–844. <https://doi.org/10.1182/blood.2019004446>.
- Zhou, F., Li, X., Wang, W., Zhu, P., Zhou, J., He, W., Ding, M., Xiong, F., Zheng, X., Li, Z., et al. (2016). Tracing haematopoietic stem cell formation at single-cell resolution. *Nature* 533, 487–492. <https://doi.org/10.1038/nature17997>.
- Zhu, Q., Gao, P., Tober, J., Bennett, L., Chen, C., Uzun, Y., Li, Y., Howell, E.D., Mumau, M., Yu, W., et al. (2020). Developmental trajectory of pre-hematopoietic stem cell formation from endothelium. *Blood* 136, 845–856. <https://doi.org/10.1182/blood.2020004801>.

STAR★METHODS

KEY RESOURCES TABLE

REAGENT or RESOURCE	SOURCE	IDENTIFIER
Antibodies		
PE-anti-TER119	BD Biosciences	Cat#: 553673; RRID:AB_394986
APC-anti-TER119	BD Biosciences	Cat#: 557909; RRID:AB_398635
PE-anti-B220 (RA3-6B2)	BD Biosciences	Cat#: 553089; RRID:AB_394619
APC-anti-B220 (RA3-6B2)	BD Biosciences	Cat#: 553092; RRID:AB_398531
PE-anti-Gr1 (RB6-8C5)	BD Pharmingen	Cat#: 553128; RRID:AB_394644
PE-anti-CD48 (HM48-1)	BD Pharmingen	Cat#: 557485; RRID:AB_396725
PE-anti-CD3e (17A2)	BD Pharmingen	Cat#: 555275; RRID:AB_395699
APC-anti-CD150 (TC15)	Biolegend	Cat#: 115909; RRID:AB_493461
PE-Cy7-anti-SCA-1 (D7)	BD Biosciences	Cat#: 558162; RRID:AB_647253
Alexa Fluor 700-anti-SCA-1	eBioscience	Cat#: 56-5981-82; RRID:AB_657836
APC-eFluor 780-anti-c-Kit (CD117) (2B8)	eBioscience	Cat#: 47-1171-82; RRID:AB_1272177
APC-anti-c-Kit (2B8)	BD Biosciences	Cat#: 553356; RRID:AB_398536
Purified anti-c-Kit	Abcam	Cat#: ab256345; RRID:AB_2891166
PE-Cy7 anti-CDH5 (CD144, VE-cadherin)	BioLegend	Cat#: 138015; RRID:AB_2562885
APC-Ki67 (20Raj1)	eBioscience	Cat#: 17-5699-42; RRID:AB_2573218
APC anti-CD45	BD Pharmingen	Cat#: 559864; RRID:AB_398672
APC-Cy7-anti-Ly-6G and Ly-6C (RB6-8C5)	BD Pharmingen	Cat#: 557661; RRID:AB_396775
PE-anti-CD8a (53-6.7)	BD Biosciences	Cat#: 553032; RRID:AB_394570
PE-anti-CD4 (Gk1.5)	BD Pharmingen	Cat#: 557308; RRID:AB_396634
PE-anti-CD31 (MEC 13.3)	BD Biosciences	Cat#: 553373; RRID:AB_394819
PE-Annexin V	BD Biosciences	Cat#: 556421; RRID:AB_2869071
Purified-anti-c-Kit (2B8)	eBioscience	Cat#: 14-1171-85; RRID:AB_467434
Purified-anti-c-Kit (D13A2)	Cell Signaling Technology	Cat#: 3074; RRID:AB_1147633
Purified-anti-c-Kit (rabbit)	Abcam	Cat#: ab256345; RRID:AB_2891166
Purified anti-GM130	BD Biosciences	Cat#: 610823; RRID:AB_398142
Anti-GRASP55 Rich	Kind gift from Dr. Bekier and Prof. Rabouille (Hubrecht Institute)	N/A
Anti- α -tubulin (rat)	Abcam	Cat#: ab6160; RRID:AB_305328
Anti- β -tubulin (mouse)	Sigma	Cat#: T8328; RRID:AB_1844090
biotinylated anti-CD31 (MEC 13.3)	BD Biosciences	Cat#: 553371; RRID:AB_394817
Anti-phospho-AKT-Ser473	Cell Signaling	Cat#: 4060; RRID:AB_2315049
Anti-pan-AKT	Cell Signaling	Cat#: 4691; RRID:AB_915783
Alkaline phosphatase Anti-Digoxigenin-AP, Fab fragments	Roche	Cat#: 11093274910; RRID:AB_514497
Alexa Fluor™ 647 goat anti-rabbit IgG (H+L)	Life Technologies Europe BV	Cat#: A21245; RRID:AB_2535813
Alexa Fluor™ 488 goat anti-rabbit IgG (H+L)	Life Technologies Europe BV	Cat#: A11008; RRID:AB_143165
Alexa Fluor™ 594 goat anti-rat IgG (H+L)	Life Technologies Europe BV	Cat#: A11042; RRID:AB_2534099
Streptavidin Alexa Fluor® 555 conjugate	Life Technologies Europe BV	Cat#: S-21381
Horseradish Peroxidase (HRP) -conjugated secondary antibodies	GE Healthcare	Cat#: NA934; RRID:AB_772206 (donkey anti-Rabbit), Cat#: NA931; RRID:AB_772210 (sheep-anti mouse), Cat#: NA935; RRID:AB_772207 (goat - anti rat)

(Continued on next page)

Continued

REAGENT or RESOURCE	SOURCE	IDENTIFIER
EasySep™ Mouse Hematopoietic Progenitor Cell Isolation Kit (FL custom-made kit, not containing antibodies against CD11b)	STEMCELLtechnology	Cat#: BM #19856
Chemicals, peptides, and recombinant proteins		
E3 medium	Hubrecht Institute	N/A
MethoCult™ M3434 medium	StemCell Technologies	Cat#: 03434
MyeloCult M5300	StemCell Technologies	Cat#: 05350
α-MEM	Gibco	Cat#: 12571063
DMEM (Dulbecco's modified Eagle's medium)	Gibco	Cat#: 31331-028
1x MEM non-essential amino acids	Gibco	Cat#: 12084947
Neomycin Sulfate	Sigma	Cat#: 1405-10-3
IOtest® 3 Lysing Solution	Beckman Coulter	Cat#: A07799
Hoechst 33258, pentahydrate (bis-benzimide)	Invitrogen	Cat#: H3569
7-AAD (7-Aminoactinomycin D)	Invitrogen	Cat#: A1310
Recombinant murine IL-3	BD Pharmingen	Cat#: 554579
Recombinant Murine SCF	Peprotech	Cat#: 250-03
Recombinant Murine SCF	Stem Cell Technologies	Cat#: 78064
Recombinant Murine Flt3-Ligand	Peprotech	Cat#: 250-31L-10ug
1-phenyl-2-thiourea, PTU	Sigma-Aldrich	Cat#: P7629-25G
NotI GQ, 1,000u	Promega	Cat#: R6435
Ethyl 3-aminobenzoate methanesulfonate salt Tricaine, MS-222	Sigma-Aldrich	Cat#: A5040-25G
Ethyl 3-aminobenzoate methanesulfonate	Sigma	Cat#: E10521
UltraPure™ Agarose	Invitrogen	Cat#: 16500-500
Paraformaldehyde (PFA)	Sigma-Aldrich	Cat#: P-6148
TWEEN 20	Sigma-Aldrich	Cat#: P1379-100ML
Proteinase K, 100 mg	Promega	Cat#: V3021
Bovine serum albumin (BSA)	Sigma-Aldrich	Cat#: A3294-100G
Glycerol, 'Baker Analyzed'	Boom Laboratoriumleverancier	Cat#: MBAK7044.2500
Acridine orange (AO)	Kind gift from Prof. Bakkers (Hubrecht Institute)	N/A
Penicillin-Streptomycin (5,000 U/mL)	Life Technologies	Cat#: 15070063
Collagenase	Sigma-Aldrich	Cat#: C0130-1G
Trypan Blue Solution, 0.4%	Life Technologies Europe BV	Cat#: 15250-061
Goat serum	Sigma-Aldrich	Cat#: S26-LITER
TrypLE	Gibco	Cat#: 12604054
EDTA	Hubrecht Institute	N/A
1X protease inhibitor (EDTA-free)	Roche	Cat#: 11836145001
DAPI	Sigma-Aldrich	Cat#: D9542-10MG
RQ1 RNase-Free DNase, 1,000u	Promega	Cat#: M6101
GoTaq G2 Flexi DNA Polymerase, 500u	Promega	Cat#: M7805
iQ™ SYBR® Green Supermix	Bio-Rad	Cat#: 1708880
iTaq Universal SYBR Green Supermix	Bio-Rad	Cat#: 1725122
SYBR Green	Roche	Cat#: 04707516001
Hydrocortisone 21-hemisuccinate sodium salt	Sigma-Aldrich	Cat#: H2270-100MG
0.8% low-melting agarose	Invitrogen	Cat#: 16520050
PBS Dulbecco's Phosphate Buffered Saline	Sigma-Aldrich	Cat#: D8537
NBT	Sigma-Aldrich	Cat#: 11383213001
BCIP	Sigma-Aldrich	Cat#: 11383221001
OCT medium	Sakura	Cat#: 4583

(Continued on next page)

Continued

REAGENT or RESOURCE	SOURCE	IDENTIFIER
HEPES	ThermoFisher	Cat#: 15630080
Protease Inhibitor Cocktail	Thermo Scientific	Cat#: A32955
Bafilomycin A1 (BafA, 100nM)	Invitrogen	Cat#: tlr-baf1
Tunicamycin	Sigma-Aldrich	Cat#: T7765
Fetal calf serum	Sigma	Cat#: F7524
L-Glutamine 200 mM (100ml)	Life Technologies	Cat#: 25030-024
L-Glutamine	Invitrogen	Cat#: 25030-032
Sodium pyruvate	ThermoFisher	Cat#: 11360070
Sodium pyruvate	Invitrogen	Cat#: 11360-039
2 -mercaptoethanol (0.1mM)	Gibco	Cat#: 11528926
Non-fat powder milk	Sigma	Cat#: 70166-500G
PVDF membranes	Millipore	Cat#: IPVH00010
LIF	Sigma-Aldrich	Cat#: PD0325901
CHIR	Tocris Biochemicals	Cat#: 4423-10
PD	Stemgent	Cat#: 04-0006
Endo H	NEB	Cat#: P0702S
Pngase F	NEB	Cat#: P0704S
IRDyes 800CW and 600CW	Li-cor	N/A
Enhanced chemiluminescence detection (ECL)	GE Healthcare	Cat#: RPN2236
Fluorescent detection (Odyssey Imaging System)	Licor	Cat#: 926-68071 (goat anti-rabbit, IR dye 680 CW) Cat#: 926-32210 (goat anti-mouse, IR dye 800 CW)
Ambion MEGAscript T7 transcription kit	Life Technologies	Cat#: AM1333
pCS2-nCas9 n plasmid	Addgene	Cat#: 47929
Clasp2 morpholino	GeneTools, LLC	N/A
pCS2+ plasmid	Kind gift from Prof. den Hertog (Hubrecht Institute)	N/A
BD Cytotfix/Cytoperm™	BD Bioscience	Cat#: 554714
RNeasy Mini kit	Qiagen	Cat#: 74104
SuperScript® III Reverse Transcriptase	Life Technologies	Cat#: 18080044
SuperScript® IV Reverse Transcriptase	Thermo Fisher	Cat#: 18-090-050
GFP-GM130 mRNA	(Pouthas et al., 2008) mRNA kindly provided by Prof. Bakkers (Hubrecht Institute)	N/A

Experimental models: Organisms/strains

Mouse: C57BL/6J (CD45.2)	The Jackson Laboratory	JAX: 000664
Mouse: Clasp2 ^{+/-} (C57BL/6)	Kind gift from Prof. Galjart (ErasmusMC, Rotterdam, NL)	(Drabek et al., 2012)
Zebrafish: <i>mpeg1.4:mCherry/mpx:eGFP</i>	This paper	N/A
Zebrafish: <i>cd41:eGFP/kdr:mcherry</i>	This paper	N/A
Zebrafish: <i>cd41:eGFP/kdr:mcherry/clasp2mut[-4bp]</i>	This paper	N/A
Zebrafish: <i>cd41:eGFP/kdr:mcherry/clasp2mut[-10bp]</i>	This paper	N/A
Zebrafish: <i>clasp2mut[-4bp]</i>	This paper	N/A
Zebrafish: <i>clasp2mut[-10bp]</i>	This paper	N/A
Zebrafish: AB	EZRC	Item #: 1175.1
Zebrafish: TL	EZRC	Item #: 1174.1

(Continued on next page)

Continued

REAGENT or RESOURCE	SOURCE	IDENTIFIER
MS-5 stromal line	Kind gift from Drs. Dusanter and Lauret (Cochin Institute)	N/A
Oligonucleotides		
Morpholinos	GeneTools, LCC	N/A
Primers for genotyping, CRISPR/Cas9 genome editing, semi-quantitative PCR, RT-qPCR, RT-PCR, ISH, see Table S1	IDT	N/A
Software and algorithms		
Excel	Microsoft	N/A
Fiji (ImageJ)	Fiji	https://fiji.sc
FlowJo	FlowJo	https://www.flowjo.com/
Prism7	GraphPad Software	GraphPad Software
Imaris X	Oxford Instruments	N/A
CellQuest software	BD Bioscience	N/A
CytExpert software	Beckman Coulter	N/A
Chopchop	N/A	https://chopchop.cbu.uib.no/
SnapGene	GSL Biotech LLC	N/A
Ensembl	EMBL-EBI	https://www.ensembl.org/index.html
Other		
LSM700 Confocal Microscope	Zeiss	N/A
Leica fluorescent stereomicroscope MZ 16 FA	Leica	N/A
Leica SP8 confocal microscope	Leica	N/A
Aria III flow cytometer	BD Bioscience	N/A
FACSCalibur	BD Bioscience	N/A
Jazz BD FACSJazz	BD Bioscience	N/A
FACSDiva	BD Bioscience	N/A
BD Influx Cell Sorter	BD Bioscience	N/A
CytoFLEX benchtop flow cytometer	Beckman Coulter	N/A
Hamamatsu Flash4 LT digital camera	Hamamatsu	N/A
BIO-RAD C1000 Touch Thermal Cycler, CFX384TM Real-Time System	BIO-RAD	N/A
ThermalSealRT™	Greiner	Cat#: 676044
SAPPHIRE MICROPLATE, 384 WELL	Greiner	Cat#: 785201
Mmessage Mmachine Sp6 Kit	Thermo Fisher Scientific	Cat#: 10086184
Four-well imaging dish (Muwells)	(Weijts et al., 2017)	N/A
Cell strainers 40 um Blue	VWR	Cat#: 734-0002
Adhesion slides, SuperFrost Plus	VWR	Cat#: 631-0108
Durapore® Membrane Filters (0.65 µm)	Millipore	Cat#: DVPP02500

RESOURCE AVAILABILITY

Lead contact

Further information and requests for resources and reagents should be directed to and will be fulfilled by the lead contact, Catherine Robin (c.robin@hubrecht.eu).

Materials availability

This study did not generate new unique reagents.

Data and code availability

- All data reported in this paper will be shared by the [lead contact](#) upon request.
- This paper does not report original code.
- Any additional information required to reanalyze the data reported in this paper is available from the [lead contact](#) upon request.

EXPERIMENTAL MODEL AND SUBJECT DETAILS

Animals

All animals were housed and bred according to institutional guidelines, and procedures were performed in compliance with Standards for Care and Use of Laboratory Animals with approval from the Erasmus MC and Hubrecht Institute ethical review board. All animal experiments were approved by the Animal Experimentation Committee (DEC) of the Royal Netherlands Academy of Arts and Sciences.

Mice and embryos

Clasp2^{+/-} animals (Drabek et al., 2012) were backcrossed more than 20 generations in the C57BL/6 background. Of note, the second exon common to all known isoforms of CLASP2 was interrupted by insertion of an eGFP-loxP-pMC1NEO-loxP cassette to generate the *Clasp2* mutant mice (Drabek et al., 2012). *Clasp2*^{+/-} and *Clasp2*^{-/-} embryos were generated by timed mating of *Clasp2* heterozygous transgenic males and females. The day of an observed vaginal plug was considered as embryonic day 0 (E0). Embryos (males and females) were collected at early E10 (26–32 somite pairs (sp)), E10.5 (33–36 sp), E11.5 (44–48 sp), E12.5 and E14. E10.5 and E11.5 embryos were staged based on the number of sp. Postnatally sacrificed newborn animals were staged based on the day post birth (P8). Young adult mice were 4.5 weeks old and adult mice were >8 weeks old (males and females were used).

Zebrafish and embryos

Zebrafish were maintained and propagated according to the standard laboratory conditions of the Hubrecht Institute and FELASA guidelines. For microscopic observations *clasp2* mutants (*clasp2*mut with [-4bp] and [-10bp] mutations) and wild-type fish of the reporter line Tg(*kdr1*:mCherry/*cd41*:eGFP) were used (*kdr1*:mCherry (ZFIN ID: ZDB-TGCONSTRUCT-110127-23); *cd41*:eGFP (Lin et al., 2005)). *In situ* hybridizations were done on *clasp2*mut in wild-type TL/AB (EZRC), Tg(*kdr1*:mCherry) or Tg(*kdr1*:mCherry/*cd41*:eGFP) background. For flow cytometry, embryos of the Tg(*mpeg1.4*:mCherry/*mpx*:eGFP) line (Tg(*mpeg1.4*:mCherry-F)^{ump2} (Bernut et al., 2014), and TgBAC(*mpx*:GFP)ⁱ¹¹⁴ (Renshaw et al., 2006) were used. Zebrafish embryos were raised in E3 medium and staged as described in (Kimmel et al., 1995; Westerfield, 2000) to obtain 40 h post-fertilization (hpf), 52hpf, 3 days post-fertilization (dpf) and 5dpf embryos. For *in situ* hybridization and imaging, embryos were grown from 24hpf onwards in E3 with 0.003% 1-phenyl-2-thiourea to inhibit pigment formation (Westerfield, 2000).

METHOD DETAILS

Generation of *clasp2* mutant lines by CRISPR/Cas9-mediated mutagenesis

Using chopchop web tool (<https://chopchop.cbu.uib.no/>), sgRNAs were designed to target exon 3 in iso1 *clasp2*-001 or -205 (ensemble ENSDART00000144557.3) NM_207072, exon 8 in iso2 *clasp2*-002 or -202 (ENSDART00000136873.3) NM_001328259, exon 2 in iso8 *clasp2*-008 or -208 (ENSDART00000151086.2) and exon 1 in iso4 *clasp2*-004 or -204 (ENSDART00000139109.3). The sgRNA (GGATGGAAGCAGGCCGTCAT) was chosen. SgRNA were generated strictly following the guidelines previously described in (Gagnon et al., 2014); the Ambion MEGAscript T7 kit (Life Technologies) was used for synthesis. The capped Cas9-mRNA was generated from pCS2-nCas9 n (Addgene) plasmid by linearization with NotI enzyme (Promega) and synthesized using the SP6 mMessage Machine kit (Thermo Fisher Scientific). CRISPR mutants were generated by co-microinjection of the purified sgRNA (25 ng/μL) and Cas9 mRNA (150 ng/μL) into the cell of a one-cell-stage embryo. Successful editing was assayed in the F1 offspring (F0 founder outcrossed to wild-type) by PCR (primers: 5'-ccttttcgtgcagcttatgtca-3'; 5'-ggtaattgggcaaatcattgct-3') and sequencing of the target sequence. We obtained two *clasp2* mutants with frameshift mutations (-4 bp, -10 bp). All analyses were performed on generations > F2. *Clasp2*mutant[-4bp] and [-10bp] lines were maintained and bred as described above for further analysis.

Zebrafish genotyping

DNA was isolated from embryos or fin clips of adult single fish and genotyped by PCR with primers amplifying the genomic region containing exon 3 and one designed complementary to the edited region (primers see above, and 5'-GAAGCAGGCCGT CATCGGC-3').

Morpholino and mRNA injections

The morpholino (MO) targeting the exon 1/2/3/8 splice site of *Clasp2* (sequence: ACTACGGTCTACAAGAAGCAGTGAG) was purchased from GeneTools, LCC. The 1 nL [5 ng/embryo] MO was microinjected in the yolk of 1–2 cell stage embryos. Splice-blocking MO-mediated knockdown was validated by RT-PCR for intron retention.

Full length zebrafish *clasp2* (NM_207072) was cloned in the pCS2+ (kind gift from Prof. den Hertog's laboratory, Hubrecht Institute) and fused C-terminally to mScarlet. Full length mRNA was synthesized using the SP6 message machine kit (thermofisher) and 1 nL of a 1000 ng/ μ L solution was injected in *clasp2* mutants for rescue experiments. Successfully injected embryos were selected based on mScarlet expression at 24hpf. The embryos were analyzed at 3dpf for a curved body axis and imaged with Leica stereomicroscope MZ16FA with a Hamamatsu Flash4 LT digital camera and fixed for *cmyb* WISH. One nl of a 50-100 ng/ μ L solution GFP-GM130 (Pou-thas et al., 2008) mRNA (kindly provided by the Bakkers' laboratory, Hubrecht Institute) was injected at one cell stage into WT and *clasp2* mutant embryos. Embryos were selected based on GFP fluorescence at 28hpf and imaged at 2dpf embedded in a four-well imaging dish (Muuwells) with a Leica SP8 confocal microscope and a 63x/1.4 oil lens. Golgi integrity was analyzed using Fiji measurement and cell counting plugins on a single plane fluorescent image.

Confocal fluorescence imaging of live zebrafish embryos

Fluorescent confocal microscopy images were acquired using a Zeiss LSM700 or Leica SP8 microscope. Embryos were anesthetized with 1x tricaine (0.16 mg/mL ethyl 3-aminobenzoate methanesulfonate; Sigma E10521), mounted in 0.8% low-melting agarose (Invitrogen) in a 35 mm glass bottom dish and covered with E3 solution containing 1x tricaine. For higher magnifications, embryos were placed into a modified Four-Well WillCo dish (Weijts et al., 2017) covered with 0.8% low-melting agarose and imaged with a 63x objective.

Whole-mount *in situ* hybridization on zebrafish embryos

The zebrafish antisense *in situ* hybridization (ISH) probes *runx1*, *cmyb* and *rag1* were kindly provided by Dr. Romualdo Ciau-Uitz (Prof. Roger Patient's Laboratory) and Prof. den Hertog's Laboratory. All other ISH probes (e.g., for *clasp2*) were generated by PCR amplification of a part of the coding region from template cDNA and subsequently cloned into pCS2+ plasmid (Addgene). After linearization, riboprobes were transcribed from the T7 promoter incorporating digoxigenin-11-UTP for detection via antibodies. Briefly, zebrafish embryos were collected, fixed overnight in 4% paraformaldehyde (PFA, Sigma-Aldrich) and then stepwise dehydrated in methanol before storage at -20°C . For the ISH, embryos were stepwise rehydrated in PBS with 0.1% Tween 20 (PBST, Sigma-Aldrich), incubated for 3-10 min (min.) in Proteinase K (10 μ g/mL, Promega) solution and re-fixed in 4% PFA for 20 min. The overnight incubation at 70°C with the anti-sense riboprobe in hybridization buffer (hyb) with tRNA and heparin was preceded by equilibration in hyb for >1 h. After hybridization, the embryos were stepwise washed into Sodium Salt Citrate (SSC) and then PBST, followed by a blocking step with BSA (Sigma-Aldrich) and sheep serum for 1 h. Incubation with anti-digoxigenin antibody conjugated to alkaline phosphatase was performed overnight at 4°C , followed by extensive washing with PBST and transfer into PBST. For the enzymatic detection, embryos were moved in NBT/BCIP substrate buffer. Stained embryos were fixed in 4% PFA, washed and stepwise transferred into 80% glycerol/PBS for imaging and storage. Embryos were imaged using a Leica stereomicroscope MZ16FA with a Hamamatsu Flash4 LT digital camera.

Acridine orange staining

To visualize apoptotic cells in living embryos, embryos were stained at 40hpf, 52hpf and 3dpf with the vital dye acridine orange (AO [Sigma], kindly provided by Prof. Bakkers' Laboratory, Hubrecht Institute). Embryos were placed in AO solution (10 μ g/mL) in E3 medium for 30 min and then repeatedly washed with E3 medium before embedding and imaging with the Zeiss LSM700 confocal microscope.

Mouse embryo collection, tissue dissection and cell preparation

E11 AGM regions and E14 FLs were dissected and dissociated as previously described in (Robin and Dzierzak, 2005). Briefly, embryos were removed from the uterus and separated from the placenta and YS. Dissections were performed in PBS supplemented with 10% fetal calf serum (FCS), penicillin (100 U/mL, Life Technologies) and streptomycin (100 mg/mL, Life Technologies) (PBS/FCS/PS). For AGM isolation, head and tail were cut from the trunk with needles, the peripheral blood was flushed from the aorta and the AGM was dissected. YS were separated from vitelline vessels. AGM and YS were digested 1 h in a 0.125% collagenase solution (Sigma-Aldrich) at 37°C and dissociated by multi-pipetting to obtain a single-cell suspension. FLs were mechanically crushed through 40 μ m mesh cell strainers (VWR) and resuspended in PBS/FCS/PS. P8 neonates were euthanized and dissected in PBS/FCS/PS to isolate the limb bones and spleen. BM cells were isolated from femur, tibiae, pelvic bones and humerus by gently squeezing the entire marrow out of the bone after carefully removing muscles, tendons, and periosteum from its surface. Cells were filtered through 40 μ m mesh cell strainers and resuspended in PBS/FCS/PS. The BM of young and adult mice was obtained from femur and tibiae by cutting the bone and flushing the BM out by means of a syringe with PBS/FCS/PS. Spleens, lymph nodes and thymus were mechanically crushed through 40 μ m mesh cell strainers and resuspended in PBS/FCS/PS. Cells were then washed and counted after Trypan Blue (Life Technologies Europe BV) addition (to exclude dead cells) in a Bürker Türk chamber.

Whole-mount immunostaining on mouse embryos

The developmental stage of the embryos was precisely determined by counting the numbers of somite pairs (according to the Edinburgh Mouse Atlas). E10.5 embryos were fixed, stained and mounted as previously described (Yokomizo and Dzierzak, 2010). Briefly, embryo caudal halves were dissected and the blood present in the dorsal aorta flushed out as described in (Boisset et al., 2011). Caudal halves were fixed in PBS/PFA (2%) solution for 20 min. at 4°C , washed twice in PBS and dehydrated in 100% methanol. Immunostainings were performed in PBS containing 1% skimmed milk, 0.2% bovine serum albumin, 0.4% TritonX-100 and

0.1% goat serum (PBS-MT, Sigma-Aldrich). Stainings were performed with anti-c-Kit (2B8) and biotinylated anti-CD31 (MEC 13.3) primary antibodies, and goat anti-rat Alexa Fluor 647 and Alexa Fluor 555-streptavidin secondary antibodies. All antibodies used in this study (including the source and catalogue numbers) are listed in the [key resources table](#).

Immunostaining of mouse embryo cryosections

Embryos were isolated at E10.5. Head and tail were cut off and the blood flushed out of the aorta as described above. After fixation in 4% PFA for 1 h, embryos were washed in PBS and incubated in 15% sucrose buffer overnight for cryoprotection. Embryos were transferred in 7.5% gelatin/15% sucrose solution and incubated at 37°C before placing them in a mold and freezing them in an isopentane bath on liquid nitrogen. Cryosections were cut at 10 μm thickness and collected on Superfrost slides (VWR). They were rehydrated in PBS and incubated for 1 h at 37°C for gelatin removal. Antigen-retrieval was achieved by heating the slides in 10 mM sodium citrate buffer (pH6) at 85°C for 20 min with another 20 min cool-down. For immunofluorescence of cell surface proteins (e.g., c-Kit), E10.5 embryos were fixed for 30 min in 2% PFA, washed in PBS and incubated in 15% sucrose buffer overnight for cryoprotection. Embryos were then transferred into OCT medium and frozen in a 100% ethanol bath on liquid nitrogen. Cryosections were cut at 10 μm thickness and collected on Superfrost slides (Thermo). No antigen-retrieval was required. The sections were first washed in PBS demi, then permeabilized in a 0.1% Tween20 (Sigma)/PBS demi solution and blocked in PBS-block (0.4% TritonX-100, 0.2% BSA, 0.1% goat serum) solution for 1 hour. The primary antibody (e.g., c-Kit) was incubated overnight in PBS-block at 4°C. After a washing step in PBS demi, the secondary antibody (e.g., Alexa Fluor 488 goat anti-rabbit) was incubated for 1 h at room temperature (RT) in the dark. Sections were washed, stained in DAPI (Thermo Scientific) solution, and mounted in 50% Glycerol/PBS.

Confocal microscopy imaging of mouse whole-mount embryos and cryosections

Microscopic observations of whole-mount embryo caudal halves were performed using a Zeiss LSM700 confocal microscope (Carl Zeiss), equipped with a ×10.0 fluar dry lens (numerical aperture 0.5 M27). Images were obtained using sequential scans. The Alexa Fluor 555 (AF555) fluorescence was detected using a 10.0 mW diode 555 nm and a 560–635 band pass emission filter. The Alexa Fluor 647 (AF647) fluorescence was detected using a 5.0 mW diode 639 nm and a dichromatic beam splitters 640 long pass filter. Embryo caudal halves were stained with individual antibody to check that no fluorescent signals were detected in the other channels. c-Kit expressing cells inside the aorta (delimited by CD31 expression) were counted and scored as cluster cells with the Zeiss Blue software.

The immunostained cryosections were imaged with a Leica SP8 or SP5 confocal microscope using a 63x oil lens (HC PL APO CS2 6 x/1.40 oil). Images were analyzed using Fiji (ImageJ) software tools ([Schindelin et al., 2012](#)) to measure the spread and number of objects of GM130 and GRASP55 signals.

Generation of *Clasp2*^{−/−} embryonic stem cells (ESCs)

For the generation of *Clasp2*^{−/−} ESCs, E3.5 blastocysts were flushed out from the uterus of *Clasp2*^{+/−} females crossed with *Clasp2*^{+/−} males. Each blastocyst was transferred to a single well of a 96-well plate seeded with irradiated feeder MEFs. After 6 days, cells were trypsinized and expanded into a 24-well plate with feeders. Four days later, cells were expanded into 12-well plates, and simultaneously used for extraction of genomic DNA followed by PCR to determine the genotype. After confirmation of genotype, cells were further expanded for one more passage prior to karyotyping and freezing down. 2i was added to the medium at all times.

GM130, GRASP55, LAMP-1 and c-kit immunostaining and quantification

Spread and/or number of GM130⁺ and GRASP55⁺ Golgi objects, and LAMP-1 lysosomal vesicles, were measured and counted using the Fiji measuring tool and plugin cell counter on immunofluorescent images of the respective antibody staining. For measuring Golgi size, in ESCs (GM130 staining), confocal z-stacks were first converted to maximum intensity projections to capture the entire Golgi network. The Golgi was outlined manually as a ROI using the freehand selection tool in Fiji and the total area of this ROI was then calculated.

Image quantifications for c-Kit were done in Fiji on confocal acquired z-stacks of whole-mount embryos stained with c-Kit and CD31 antibodies. All images were acquired with identical settings. The entire membrane surface of each IAHC cell as stained by c-Kit inside the aorta (CD31⁺), was outlined using a segmented line ROI of width 2 pixels (0.62 μm) to include the plasma membrane, as well as 1 pixel on either side of it. The average c-Kit fluorescence intensities were measured using a custom-made ImageJ plugin, which facilitated manual annotation of the circumference of IAHC cells and automatic estimation of parameters such as background intensity around a cell, average intensity along the circumference (within a narrow band with a thickness of 0.62 μm) and minimum intensity within the cells (the corresponding regions are marked as “outside”, “plasma membrane” and “inside” in [Figure 5](#)). For each developmental time point, cells were manually annotated in 3D image stacks. For each cell, the annotation was done in its focal plane (the corresponding z-slice of the 3D image stack, also checking the CD31 signal) by drawing a 2D contour (as a region of interest (ROI)) and adding to the ImageJ's ROI Manager. All the ROIs were further automatically processed to extract the abovementioned parameters using a custom-made plugin. For intersecting ROIs, the overlapping parts of the contours were properly accounted for while computing the averages.

Flow cytometry analysis and cell sorting

For zebrafish

Embryos were sorted at 3dpf based on transgene expression and anesthetized using tricaine. Most of the yolk was mechanically removed with needles before collection. The remaining residues were stripped by incubation and pipetting in calcium free Ringer's solution and washing with PBS0. Embryos were then dissociated by incubation in TrypLE (Gibco), shaking at 800 rpm for 1 h at 32°C and subsequent pipetting. Before flow cytometry analysis, cells were resuspended in PBSMQ containing 2 mM EDTA, 2% sterile filtered FCS and 0.5 µg/mL DAPI (Sigma-Aldrich). Samples were acquired on a CytoFLEX cytometer and reanalyzed using the FlowJo software.

For mouse

Flow cytometry analysis and cell sorting were performed on a FACScalibur, ArianIII, Jazz BD FACSJazz, BD Influx Cell Sorter (BD Bioscience) or CytoFLEX benchtop flow cytometer (Beckman Coulter) with CellQuest (BD Bioscience), FACSDiva, BD FACS and CytExpert (Beckman Coulter) software, respectively. Stainings were performed in PBS/FCS/PS for 30 min. at 4°C. Cells were washed, suspended in PBS/FCS/PS and stained with 7-AAD (1 mg/mL, Invitrogen) or Hoechst 33258 (1 mg/mL, Invitrogen) to exclude dead cells. Isotype-matched control antibodies were used for controls. The following monoclonal antibodies (BD Pharmingen, eBioscience, Invitrogen) were used: Lin cocktail (PE-anti-Ter119, PE-anti-B220, PE-anti-Gr1, PE-anti-CD3e); PE-anti-CD48; APC-anti-CD150, Alexa Fluor 700-anti-SCA-1 or PE-Cy7-anti-SCA-1, APC-eFluor 780-anti-c-Kit or APC-Cy7-anti-c-Kit or APC-anti-c-Kit, PE-anti-CD31, and PE-anti-Ter119. For multilineage repopulation analysis, spleen cells were stained with APC-anti-B220, PE-anti-CD8a and PE-anti-CD4; BM cells were stained with APC-anti-Ly6C and PE-anti-CD31. Doublets and dead cells were excluded from the analyses.

IAHC cells were stained by injecting APC-Cy7-anti-c-Kit and PE-anti-CD31 directly in the aorta and incubated 30 min before dissection.

For type I and type II pre-HSC staining, cells were additionally stained with APC anti-CD45 and PE-Cy7 anti-CDH5 (CD144, VE-cadherin) antibodies after dissociation. Flow cytometry analyses were performed within 1 h after the end of the staining.

For cell cycle analysis, cells were isolated and stained as mentioned above. After completing the cell surface staining, cells were fixed and permeabilized with BD Cytfix/Cytoperm kit according to manufacturer's instructions (BD Bioscience). Subsequently, fixed cells were stained with APC-Ki67 for 1 h before washing in 0.1% PBS/Triton X- solution with 0.5 µg/mL DAPI. Cells were incubated at least 45 min in the DAPI solution before analysis on a BD Influx Cell Sorter.

For pre-apoptotic analysis, E14 FL or neonate BM cell suspensions were incubated for 20 min at 4°C with directly labeled antibodies, i.e., APC anti-c-Kit. Single cell suspensions were washed twice in cold PBS and resuspended in 1X binding buffer (10 mM Hepes/NaOH, pH 7.4, 140 mM NaCl, 2.5 mM CaCl₂). To evaluate cell viability and the apoptotic status, cells were stained with Annexin V-PE and 7-AAD during 20 min. at RT. Flow cytometry analyses were performed within 1 h after the end of the staining on a FACScalibur (BD) and analyzed with the FlowJo software.

The mean fluorescence intensity (MFI) was analyzed with the FlowJo software.

Magnetic depletion of lineage marker positive cells

Lineage positive cells were depleted from E14 FL, P8 BM and young adult BM by using and following the manufacturer's instructions of the EasySep™ Mouse Hematopoietic Progenitor Cell Isolation Kit. Briefly, cells are first incubated with biotinylated antibodies (CD5, ±CD11b, CD19, CD45R/B220, Ly6G/C(Gr-1), TER119, 7-4), which bind to the lineage positive cells to be depleted. Second, streptavidin-coated magnetic particles are added to attach to the biotinylated antibodies. Using a magnet, the lineage positive cells remain in the tube while the lineage negative enriched cells are released in a new tube and kept for further flow cytometry staining or snap freezing for RT-qPCR or Western Blot analysis.

RT-PCR and RT-qPCR

For zebrafish

The yolk of the zebrafish embryos was removed, and the head region was cut. One sample typically contained 15-20 embryo tails.

For mouse

AGM and FL samples, cells were pelleted by centrifugation and the supernatant was removed.

All samples were snapfrozen in liquid nitrogen and stored at -80°C. The RNA content was isolated using the RNeasy Mini kit (Qiagen) according to manufacturers' instructions, followed by the removal of genomic DNA through DNaseI digestion (Thermo Scientific) for 30 min. at 37°C and heat-inactivation at 65°C. SuperScript III First-Strand cDNA Synthesis Kit (Invitrogen) was used for cDNA synthesis. For ESC RNA isolation, ESCs were washed with PBS and then collected in TRI Reagent (Sigma). RNA was isolated using the RNeasy Mini Kit (Qiagen). For RT-qPCR, cDNA was generated using Random Primers (Invitrogen) and Superscript IV reverse transcriptase (Thermo Fisher) according to the manufacturer's instructions. PCR reactions were run on a C1000 Thermal Cycler (Bio-Rad).

RT-PCR was performed by using GoTaq-polymerase (Promega) with the listed primers in [Table S1](#).

For RT-qPCR, SYBR Green qPCR SuperMix (Life Technologies) was used with the primers listed in [Table S1](#).

LTC-IC assay

The MS-5 stromal cell line was maintained on 25 cm² flasks in α -MEM medium supplemented with 10% FCS, 1% PS, 1 mM L-glutamine (culture medium) at 37°C and 5% CO₂ in a humidified incubator. Four days before long-term culture (LTC), MS-5 stromal cells were plated into the wells of 24 well plates in culture medium. Cell confluence was reached after 48 h of culture. The day of LTC, the culture medium was removed and replaced by myeloid long-term medium (M5300, Stemcell Technologies) supplemented with hydrocortisone (10⁻⁶ M, Sigma-Aldrich). Two hundred Lin⁻SCA-1⁺c-Kit⁺ (LSK) cells isolated either from *Clasp2*^{+/+} and *Clasp2*^{-/-} E14 FLs were added per well on the top of MS-5. Cultures were maintained at 37°C and 5% CO₂ in a humidified incubator. The medium was changed once a week. The cultures were harvested every week and replated in bulk into MethoCultTM M3434 medium (StemCell Technologies) supplemented with PS to address the presence of CFU-C. All CFU-C values were normalized to initial 100 LSK cells seeded into cultures.

In vitro clonogenic assay (CFU-C)

Colony formation capacity was tested in MethoCult M3434 medium (StemCell Technologies) supplemented with PS. Different dilutions of cells isolated from freshly dissociated AGM, AGM explants, YS, FL, or BM from *Clasp2*^{+/+} and *Clasp2*^{-/-} embryos or P8 neonates were mixed with MethoCult. The medium was then dispensed into culture dishes (triplicates) by using a syringe and blunt end needle. Plates were incubated in a humidified incubator at 37°C and 5% CO₂. Colonies were scored after 12 days using an inverted microscope and gridded scoring dishes.

Long-term in vivo transplantation assay

Cell suspensions corresponding to the embryo equivalent (ee) of one AGM or 0.001-0.005 ee of FL from *Clasp2*^{+/+} or *Clasp2*^{-/-} male embryos were intravenously co-injected with 2 × 10⁵ WT spleen cells into sub-lethally irradiated WT female recipients (C57BL/6, irradiated with a 9 Gy split-dose, ¹³⁷Cs-source). The blood of the transplanted recipients was analyzed 4 months post-transplantation for the presence of donor cell markers (*Clasp2* and/or *yml*) by semi-quantitative polymerase chain reaction (PCR). Signal quantitation was measured by DNA normalization (myogenin [*myo*]) and *Clasp2* and/or *yml* control DNA dilutions (0–100% donor marker). Recipients were considered repopulated when the chimerism in the peripheral blood was >10%.

For multilineage repopulation analysis, hematopoietic organs from primary reconstituted recipients (lymph nodes, thymus, BM, and spleens) were dissected. Erythroid, myeloid, T and/or B cells were sorted from recipient BM and spleen after antibody staining as previously described (Robin et al., 2011). To assess self-renewal capacity, BM cells isolated from primary reconstituted recipients were injected into secondary sub-lethally irradiated recipients (3 × 10⁶ cells/recipient). Percentages of chimerism in the blood were determined as previously described by semi-quantitative PCR at 4 months post-transplantation.

AGM explant culture

E11 AGMs were cultured as explants at 37°C in 5% CO₂ for 3–4 days as previously described (Medvinsky and Dzierzak, 1996). Briefly, AGMs were cultured on a filter (Durapore 0.65 μ m, Millipore) on the top of a steel mesh grid at the medium-air interface. The Myelocult medium (M5300, StemCell Technologies) was supplemented with 10⁻⁶M hydrocortisone succinate (Sigma) and 100 ng/mL SCF, Flt3L (Peprotech) and IL-3 (BD Pharmingen). After 3–4 days of culture, AGM explants were collected from the filter with a scalpel and dissociated with collagenase as previously described (Medvinsky and Dzierzak, 1996).

Culture and treatment of Lin⁻ fetal liver cells and/or embryonic stem cells (ESCs), c-Kit and glycosylation analyses

Lineage negative cells were isolated from E14 FLs by negative selection using the EasySepTM Mouse Hematopoietic Progenitor Cell Isolation Kit (as described above). The cells were cultured overnight in triplicates at 75,000 cells per well of a 24-well plate in Myelocult medium (M5300, StemCell Technologies). The medium was supplemented with 10⁻⁶ M hydrocortisone succinate (Sigma). Cells were cultured untreated, or in the presence of either 50 ng/mL SCF (Peprotech) or Bafilomycin A1 (BafA, 100 nM, Invitrogen), or both SCF and BafA. After culture, cells were harvested, stained with APC-anti-c-Kit (2B8, BD Bioscience) and analyzed by flow cytometry analysis as described above. c-Kit mean fluorescence intensities (MFI) were analyzed with the FlowJo software.

ESCs were cultured without feeders on plastic coated with 0.2% gelatin, and replated every 2–3 days at a split ratio of 1:5 following dissociation with Trypsin-EDTA. Cells were cultured in DMEM (Dulbecco's modified Eagle's medium) supplemented with 7.5% fetal calf serum (BioWest), 2 mM L-glutamine, 1 mM sodium pyruvate (both from Invitrogen), 0.1 mM 2-mercaptoethanol, 1x MEM non-essential amino acids (Gibco), 100 units/mL LIF, PD (1 μ M, PD0325901, Stemgent), CHIR (3 μ M, CHIR99021, Tocris Biochemicals). Recombinant mouse SCF (Stem Cell Technologies) was added to cultures overnight at 50 ng/mL. In some experiments, BafA (Invitrogen) was added at 100 nM for 6 h in conjunction with SCF. Tunicamycin (Sigma) was added to cells overnight, at a concentration of 1 μ g/mL before harvesting and western blotting was performed. For the glycosylation enzyme treatment, ESCs from 3 × 10 cm dishes were harvested and lysed in 200 μ L lysis buffer containing 20 mM Tris (pH7.5), 150 mM KCL, 0.5% TritonX-100, 0.2% SDS, 10% Glycerol, 1X protease inhibitor (Roche, EDTA-free), followed by clarification at 5000 rpm for 10 min at 40°C. Forty μ L of clarified lysate was used for each enzymatic reaction. Endo H and Pngase F (both from NEB) were added according to the manufacturer's instructions and reactions were incubated for 1 h at 37°C. Treated samples were then boiled with an equal volume of SDS sample buffer and western blotting was performed as described below.

Western blotting

E14 FL cells were washed in PBS after sorting, and cell pellets were snap frozen and stored in -80°C until use. Pellets were lysed in SDS sample Buffer (Laemmli, 1970) containing 2% SDS, 10% glycerol, 5% β -mercaptoethanol, 33 mM Tris pH 6.8, and Protease Inhibitor Cocktail (Roche, according to manufacturers' instructions). ESCs were scraped directly from 3.5 mm dishes in SDS sample buffer and denatured by boiling. Proteins were separated by SDS-PAGE and transferred to PVDF membranes (Millipore). Membranes were blocked in 5% non-fat powder milk (Sigma) in PBS with 0.1% Tween 20 (PBS-T) and incubated with primary antibodies overnight at 4°C . After 3 washes, membranes were incubated with Horseradish Peroxidase (HRP)-conjugated secondary antibodies (GE Healthcare) at 1:10,000 dilution or IR dyes (800CW and 600CW, Licor) at 1:15,000 dilution for one hour. Blots were visualized by enhanced chemiluminescence detection (ECL, GE Healthcare), or fluorescent detection (Odyssey Imaging System, Licor). Band intensity on blots was analyzed using the Gel Analysis Plugin in Fiji. Intensities were normalized to tubulin (loading control) intensity in each lane on the blots and in each blot the *Clasp2*^{+/+} sample at the left was considered as 100.

QUANTIFICATION AND STATISTICAL ANALYSIS

For all quantifications and statistical analyses Prism7 software (GraphPad Software, Inc.) was used. Results were expressed as mean \pm SEM or mean \pm SD. RT-qPCR data are shown as mean \pm SD. Student's t-test or Mann-Whitney U test were applied to determine the level of significance between two groups. Welch's t test was applied when the two samples to compare had unequal variances and/or unequal sample sizes. $p < 0.05$, 0.01, 0.001 and 0.0001 were considered statistically significant and marked as *, **, ***, and ****, respectively.